



Device Applications of Metafilms and Metasurfaces

**Mark Brongersma
LELAND STANFORD JUNIOR UNIVERSITY**

**11/06/2017
Final Report**

DISTRIBUTION A: Distribution approved for public release.

**Air Force Research Laboratory
AF Office Of Scientific Research (AFOSR)/ RTB1
Arlington, Virginia 22203
Air Force Materiel Command**

DISTRIBUTION A: Distribution approved for public release.

REPORT DOCUMENTATION PAGE				<i>Form Approved</i> <i>OMB No. 0704-0188</i>	
<p>The public reporting burden for this collection of information is estimated to average 1 hour per response, including the time for reviewing instructions, searching existing data sources, gathering and maintaining the data needed, and completing and reviewing the collection of information. Send comments regarding this burden estimate or any other aspect of this collection of information, including suggestions for reducing the burden, to Department of Defense, Executive Services, Directorate (0704-0188). Respondents should be aware that notwithstanding any other provision of law, no person shall be subject to any penalty for failing to comply with a collection of information if it does not display a currently valid OMB control number.</p> <p>PLEASE DO NOT RETURN YOUR FORM TO THE ABOVE ORGANIZATION.</p>					
1. REPORT DATE (DD-MM-YYYY) 31-07-2018		2. REPORT TYPE Final Performance		3. DATES COVERED (From - To) 15 Jul 2014 to 14 Jul 2017	
4. TITLE AND SUBTITLE Device Applications of Metafilms and Metasurfaces				5a. CONTRACT NUMBER	
				5b. GRANT NUMBER FA9550-14-1-0117	
				5c. PROGRAM ELEMENT NUMBER 61102F	
6. AUTHOR(S) Mark Brongersma				5d. PROJECT NUMBER	
				5e. TASK NUMBER	
				5f. WORK UNIT NUMBER	
7. PERFORMING ORGANIZATION NAME(S) AND ADDRESS(ES) LELAND STANFORD JUNIOR UNIVERSITY 450 SERRA MALL STANFORD, CA 94305-2004 US				8. PERFORMING ORGANIZATION REPORT NUMBER	
9. SPONSORING/MONITORING AGENCY NAME(S) AND ADDRESS(ES) AF Office of Scientific Research 875 N. Randolph St. Room 3112 Arlington, VA 22203				10. SPONSOR/MONITOR'S ACRONYM(S) AFRL/AFOSR RTB1	
				11. SPONSOR/MONITOR'S REPORT NUMBER(S) AFRL-AFOSR-VA-TR-2018-0286	
12. DISTRIBUTION/AVAILABILITY STATEMENT A DISTRIBUTION UNLIMITED: PB Public Release					
13. SUPPLEMENTARY NOTES					
14. ABSTRACT This is the final performance report for a program entitled: 'Device Applications of Metafilms and Metasurfaces'. The proposed effort aimed to demonstrate that the performance of such thin film optoelectronic devices can be improved by judiciously nano-patterning the constituent layers at length-scales below the wavelength of light. This action creates metafilms and metasurfaces that have optical properties that can go beyond those found in nature. We have explored how the fundamental light-matter interactions are modified from continuous unpatterned films to provide enhanced light-absorption and emission properties. We have also demonstrated photodetectors with improved performance and new optical functionalities, including subwavelength photon sorting, by wavelength and polarization					
15. SUBJECT TERMS metasurface, metafilm, light-matter interaction, subwavelength					
16. SECURITY CLASSIFICATION OF:			17. LIMITATION OF ABSTRACT UU	18. NUMBER OF PAGES	19a. NAME OF RESPONSIBLE PERSON POMRENKE, GERNOT
a. REPORT Unclassified	b. ABSTRACT Unclassified	c. THIS PAGE Unclassified			19b. TELEPHONE NUMBER (include area code) 703-696-8426

Performance Report
Device Applications of Metafilms and Metasurfaces

AFOSR Grant Number FA9550-14-1-0117
07/15/2014 to 07/14/2017

Grantee Institution: Stanford University
476 Lomita Mall
Stanford, CA 94305

Program Manager: Dr. Gernot Pomrenke,
Tel: (703) 696-8426
Email: gernot.pomrenke@afosr.af.mil

Principal Investigator: Dr. Mark L. Brongersma
Tel: (650) 736 2152
Email: Brongersma@stanford.edu



Table of Contents

- I. Executive Summary 2
 - 1. Statement of Objectives and Key Accomplishments2

- II. Research Accomplishments3
 - 1. Achieving near-unity absorption in deep subwavelength semiconductor film3
 - 2. The origin of the strong, omnidirectional absorption in ultrathin semiconductor5
 - 3. Achieving near-unity absorption in semiconductor metafilms at any wavelength10
 - 4. Building blocks for superabsorbing semiconductor films13
 - 5. Superabsorbing artificial metal films constructed from semiconductor antennas.....18
 - 6. Anti-Hermitian Photodetector Facilitating Efficient Subwavelength Photon-sorting ...29
 - 7. Cathodoluminescence Characterization of Metamaterial Building Blocks26
 - 8. References38

- III. Personnel and Training Opportunities39
 - 1. Supported personnel in the team39
 - 2. Research Training of Students39

- IV. Dissemination of Research findings40
 - 1. Publications, books, and scientific presentations40
 - 2. Interactions and transitions40
 - 3. Honors and Awards40

I. Executive summary

I.1. Statement of objectives and key accomplishments

Future military systems will utilize highly sophisticated electronic, photonic, and wireless networks to connect tactical forces with command and control. Rapid access to information via high-speed communication networks will also be essential to the Homeland Defense forces. For this reason, the United States needs to continue to lead the development of ultra-fast, low-cost, low-power functional communication systems to prevail as a nation and to provide security within our borders.

Photodetectors and optical sources are among the key optoelectronic devices that make up optical communication systems. *They are typically built up from thin, stacked films of metals and semiconductors. This proposal aims to demonstrate that the performance of such devices can be improved by judiciously nano-patterning the constituent layers at length-scales below the wavelength of light. This action creates 'metafilms' and 'metasurfaces' that have optical properties that can go beyond those found in nature¹. We will explore how the fundamental light-matter interactions are modified from continuous unpatterned films to provide enhanced light-absorption and emission properties.*

When metals or high refractive-index semiconductors are patterned at the nanoscale, the resulting nanoparticle, nanogrooves, and nanowire building blocks will support strong optical resonances whose resonant frequency can be tuned by controlling their size, shape, spacing, and spatial arrangement. When these resonant building blocks are placed together in arrays with subwavelength spacings, they can effectively be treated as metafilms and metasurfaces that can display dramatically modified optical transmission, absorption, reflection, and refraction properties. For such a treatment to be of value, it is key that the building blocks are spaced sufficiently close together to avoid the generation of diffracted orders (i.e produce grating/Bragg scattering effects). Under those conditions, the materials can be described as homogeneous materials with new, effective optical materials parameters. These effective optical properties can be controlled/tuned by controlling/tuning the optical properties of the resonant constituent building blocks.

This proposal aimed to explore how to best encode the optical response of nanoscale resonant building blocks into the effective properties of thin films and surfaces to best enhance device performance. The work explored both the opportunities and the fundamental limitations of this approach to enhance the performance of light absorbing (e.g. photodetector) devices.

Whereas the program aimed to answer fundamental questions about the design and optical properties of 2-dimensional metamaterials, we also built prototype devices in the 3rd year that demonstrate enhanced and absorption and photon sorting functions. In doing so, we demonstrated the benefits of 2-dimensional metamaterials over their 3-dimensional metamaterials in terms of their ease of fabrication and integration. This work will guide the possible implementation of metafilms in a wide variety of application beyond nanostructured photodetectors, including integrated biosensors and quantum-optics, and spectroscopy platforms.

The key objectives of the proposed effort were to :

- Explore the fundamental physics of light-matter interaction, involving strongly coupled excitations between plasmons, dielectric Mie resonances, excitons, excited charges.
- Understand the evolution of the resonant properties of metallic and semiconductor nanostructures as they are placed into dense arrays with subwavelength spacings.
- Pattern dense arrays of resonant nanogrooves into metal surfaces to realize metamaterial-mirrors whose reflection phase can be controlled to enhance light absorption and emission

processes from thin device layers.

- Pattern dense arrays of resonant semiconductor nanostructures to realize super-absorbing and super-emitting metafilms.
- Develop fabrication and integration procedures for metafilm and metasurface devices with densely intertwined metallic and semiconductor nanostructures.
- Perform simultaneous materials and optical characterization on the metafilms and metasurfaces to link the structural properties at the atomic-scale to the optical properties of a nanophotonic elements.

II. Research Accomplishments

II.1. Achieving near-unity absorption in deep subwavelength semiconductor films

Nanoscale optical microcavities can enhance and control light-matter interactions by confining light to small volumes by resonant recirculation². This control can be used to spectrally tailor and enhance light absorption and emission processes at a desired wavelength. In planar devices, the reflections that occur between layers of different refractive index or highly-reflective mirrors cause the occurrence of standing-wave resonances known as Fabry-Perot (FP) resonances. Based on the conceptual simplicity and ease of fabrication, FP resonators find application in a wide variety of devices, including photodetectors and optical sources as well as fundamental physics experiments studying cavity quantum electrodynamics. For many device applications, it would be desirable to achieve near-unity absorption in the thinnest possible semiconductor film. This would enable resource efficient devices that can be realized in short deposition times. It also could enable detectors and sources with excellent performance in terms of speed and charge extraction/injection.

Conventionally, FP resonances are tailored for a specific application by first choosing a set of materials based on some desirable set of structural, electronic and/or optical properties. These may e.g. include a materials compatibility with Si, a high charge carrier mobility, a low surface recombination velocity, or a high quantum efficiency for light emission. With knowledge of the optical properties of the materials, the thicknesses of the different layers in the device can be optimized to engineer a strong FP resonance. Mathematically, it is easy to see the importance of both the optical materials properties and physical dimensions of the structure by considering a FP resonator, consisting of a single layer of semiconductor material. For such a structure a resonance will occur when light picks up a phase equal to an integer number m of 2π when making a round trip in the cavity. The resonance condition for normally-incident light can mathematically be written as:

$$4\pi t n / \lambda + \varphi_t + \varphi_b = 2\pi m \quad \text{Eq.(1)}$$

where t is the semiconductor layer thickness, n the real part of the refractive index, λ the illumination wavelength, and φ_t and φ_b are the reflection phases for reflections from the top and bottom interfaces of the semiconductor layer. The first term in the equation above is the propagation phase, which on resonance needs to add up with the reflection phases to 2π .

Recently, the Capasso group at Harvard received significant attention for a study that showed how very strong absorption could be obtained in a very thin (~ 10 nm) semiconductor layer grown on a metallic substrate³. This structure operates as an asymmetric FP resonator known as a Gires-

Tournois (GT) resonator⁴. Conventional GT resonators clamp a transparent medium in between a partially reflective front mirror and a highly reflective back mirror. Upon illumination, such a resonator reflects virtually all the incident light, but imparts a frequency-dependent phase on the reflected wave. The Capasso group instead constructed a GT resonator by placing an absorbing germanium (Ge) layer on a gold (Au) substrate to show that this type of resonator can also be used to achieve very strong (80 - 90%) light absorption at a target wavelength of interest. This intriguing phenomenon has already been applied in the field of photocatalytic water splitting, by showing that visible light can effectively be absorbed in a deep-subwavelength iron oxide layer⁵.

Inspired by the work above, we performed preliminary calculations based on the transfer matrix method, to show that one can in fact can achieve unity, near-omnidirectional at a specific wavelength of 625 nm for a judiciously chosen Ge film thickness of 12 nm deposited on a silver (Ag) substrate (See Fig. 1a). It can also be seen that the absorption remains above around 75% over the visible regime (solid blue line).

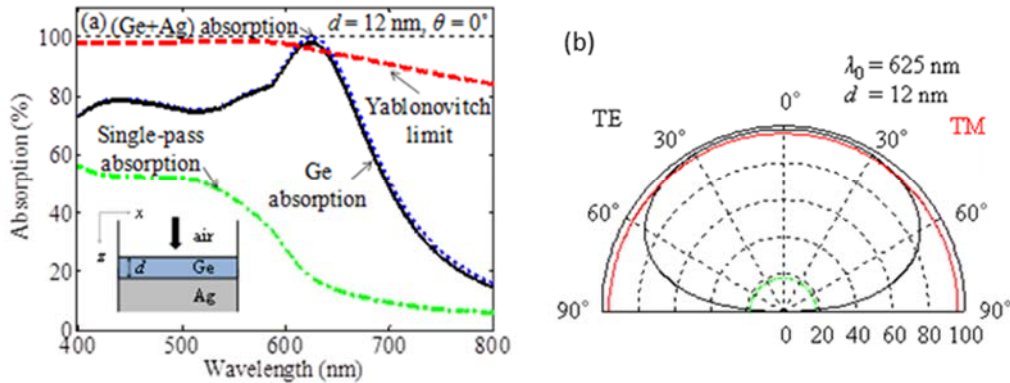


Figure 1. (a) Absorption spectrum for a layer structure consisting of air/Ge(12nm)/Ag substrate (see inset) upon illumination with normally-incident light. Dashed red line: Yablonovitch limit, dotted blue line: absorption in Ge and Ag, solid black line: absorption in just the Ge, and dash-dotted green line: single-pass absorption. (b) Angle dependence of the absorption at the wavelength of 625 nm and the thickness of 12 nm. Solid red line: Absorption in the Ge for transverse magnetic (TM), Solid black line: absorption in the Ge for transverse electric (TE) polarization, Dash-dotted green line: single-pass absorption in Ge.

At 625 nm, 98% of the incident light gives rise to useful absorption in the Ge and can produce photogenerated charge. Only 2% of the light is absorbed in the Ag film, where the light energy is dissipated in heat. This high absorption in the Ge layer cannot solely be attributed to the large, intrinsic materials absorption. To check the contribution of the material absorption, we plot the single-pass absorption (dash-dotted green line), defined as $A_{sp} = 1 - \exp(-\alpha d)$ (α : attenuation coefficient of Ge, d : Ge thickness). Note that the single-pass absorption itself does not reach 20% at the wavelength of 625 nm. Therefore, it is clear that such a high absorption in the Ge layer is to the presence of the metal substrate.

Figure 1(b) shows that the absorption in the Ge layer is very strong for both the transverse magnetic (TM) and transverse electric (TE) polarization of light. It also shows that the absorption exceeds 80% over incident angles up to 66° and 67° for TM and TE polarizations, respectively. The omni-directional absorption behavior is in part expected based on the high-index of the metal film which causes refraction towards the normal. For this reason the light always propagates quite close to the normal, irrespective of the incident angle in the air. As part of our efforts, we proposed to analyze the origin of this every strong absorption and understand the omni-directional behavior in more detail.

II.2. The origin of the strong, omnidirectional absorption in ultrathin semiconductor films

When optimizing light-matter interaction in planar, translationally-invariant systems, one typically thinks of driving a Fabry-Pérot resonance. The resonance condition for this type of resonance is that the total phase accumulation upon one roundtrip in the cavity should equal an integer-multiple of 2π ($2m\pi$, $m = 1, 2, 3, \dots$). For ultrathin devices, we consider the case for which $m = 1$. Our system with a thin film deposited on a metallic backreflector, on the contrary, is a Gires-Tournois style interferometer⁴. Figures 2a and 2b show the phase for the two orthogonal (transverse magnetic (TM) and transverse electric (TE)) polarizations. Dash-dotted red curves denote the propagation phase pickup ($2\phi_p$) in the Ge layer, dashed blue curves the reflection phase pickup at the bottom boundary (ϕ_b , from Ge to Ag layer), and dotted green curves the reflection phase pickup at the top boundary (ϕ_t , from Ge layer to air). It appears the accumulation phase ($\phi_{accu} = 2\phi_p + \phi_b + \phi_t$, depicted by the solid black curve) displays near 2π (or 360°). However, a closer look reveals that accumulation phase that maximizes the absorption is different from 2π . Rather, the differential phase, which is defined as:

$$\phi_{diff} = 2\phi_p + \phi_b - \phi_t, \quad \text{Eq.(2)}$$

(depicted by the solid cyan curve) displays the exact 2π at the angle of the critical coupling condition. This is a unique feature of a Gires-Tournois resonator that is distinct from a Fabry-Pérot resonator that requires an accumulation phase of 2π . Figure 2(c) shows a trajectory of the partial sum of the reflected waves. Here r_0 is the complex reflection amplitude of the directly reflected wave from air to Ge layer, r_1 the partial reflected wave that undergoes one round trip in the Ge layer, and r_n the partial reflected wave that has made n round trips. Owing to the strong loss in Ge layer, the phase of r_0 is not π ; instead, it displays a complex phase. As a result, the partial reflected waves do not need to be aligned having the same phase and ϕ_{accu} can be different from $2m\pi$. In addition, the condition of $\phi_{diff} = 2m\pi$ can be derived from the Airy formula:

$$r_{total} = \frac{r_{12} - r_{23}e^{2i\beta d}}{1 - r_{12}r_{23}e^{2i\beta d}}, \quad \text{Eq.(3)}$$

where r_{12} is the reflection from air to Ge layer, r_{23} the reflection from Ge to Ag, β is the longitudinal wavenumber in the Ge layer, and d the thickness of Ge layer. The unity absorption condition is met when the numerator of Eq. (3) vanishes; $r_{12} - r_{23} \exp(2i\beta d) = 0$. The phase relationship for this condition is summarized as $\phi_{diff} = 2m\pi$. Note that, in the absence of the loss, ϕ_t is zero, which indicates that the plus and minus signs for ϕ_t cannot be distinguished. Therefore ϕ_{accu} becomes the same as ϕ_{diff} .

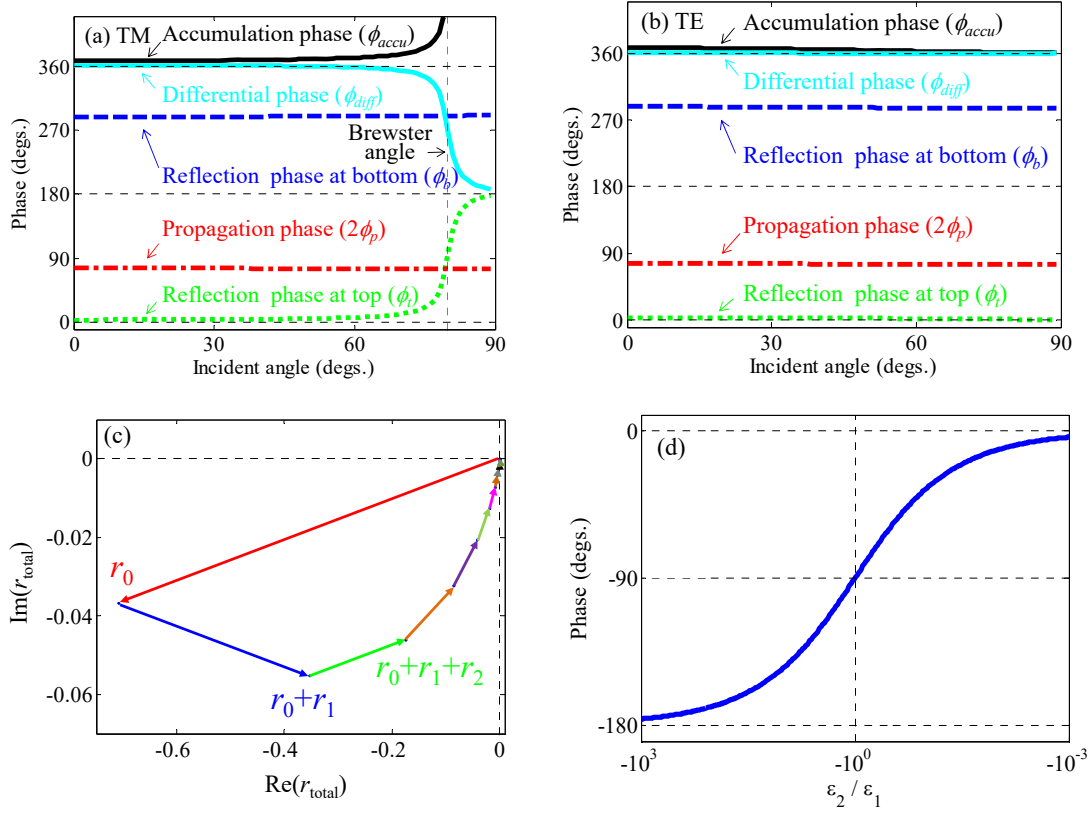


Figure 2. (a) Reflection and propagation phases as a function of the incident angle at the wavelength of 625 nm and the Ge thickness of 12 nm. Dash-dotted red line: propagation phase retardation in semiconductor, dotted green line: reflection phase pickup at the top interface (air/Ge), solid black line: total phase, and dashed blue line: reflection phase pickup at the bottom (Ge/Ag). (b) The TE result. The line legends are the same as in (a). (c) Trajectory of sums of the partial reflected waves at the critical coupling condition. (d) Reflection phase from a layer with ϵ_1 to a layer with $\epsilon_2 = \epsilon_{2,r} + i\epsilon_{2,i}$ where $\epsilon_{2,r} < 0$ and $\epsilon_{2,i} = 0$ as a function of ϵ_2 / ϵ_1 .

Each phase term remains almost constant for the wide range of incident angles. This is because the discrepancy between the indices of free space and the Ge layer is significant, and thus, according to the Snell's law, the refraction angle in the Ge layer remains very small over a wide range of incidence angles in free space. As a result, the amplitude change of the longitudinal wavenumber (in z -direction) in the Ge layer is almost zero, leading to a negligible change of phase accumulation during reflection and propagation.

The TM case has a unique transition point where the reflection phase changes at the top interface from zero to π . This point corresponds to the Brewster angle θ_B , at which TM-polarized light is perfectly transmitted (without reflection) from the air into the Ge layer. The magnitude of this angle is determined by the ratio of the refractive indices of the incident medium (air in our case) n_i and the medium that the light transmits into n_t (Ge in our case): $\theta_B = \arctan(n_t/n_i)$. If the index difference between two media is not significant, the presence of the Brewster angle in the TM case would introduce a strong dependence on the incidence angle. However, given the high index of the

Ge layer, the Brewster angle is pushed out to about 80° and the presence of the Brewster angle does not have a significant effect on the angular dependence of the light absorption.

So far, we have discussed two distinct absorption properties of the semiconductor-on-metal configuration: near-unity absorption and omni-directionality; however, the reported absorption is also significant given the extremely small thickness of the Ge layer. For example, the 12 nm-thick-Ge layer can absorb more than 98% of the light energy at the wavelength of 625 nm at normal incidence. We will argue that to achieve near-unity absorption, one need to both satisfy a destructive interference condition in the Gires-Tournois configuration and have a semiconductor layer with very strong absorption, i.e. a high imaginary part of the dielectric constant. The Gires-Tournois interference would require a thickness around $\lambda_0 / 4n_s$, where n_s is the real part of the refractive index of the semiconductor layer ($n_s = 5.5$ at $\lambda_0 = 625$ nm for Ge). It turns out that the near-unity absorption is enabled by the reflection phase pickup from the semiconductor to the metal substrate. This can be seen by analyzing the maximum absorption condition in Eq. (2) for semiconductor film exhibiting the lowest-order interference ($m = 1$) by including the phase pickups that can occur at the top and bottom interfaces: $\phi_{diff} = 2\phi_p + \phi_b - \phi_t = 2n_s k_0 d + \phi_b - \phi_t = 2\pi$, Even for strongly semiconductors, ϕ_t tends to be small (typically less than 10°) compared to the other propagation phase and reflection phase at the bottom reflector. For this reason, we ignore this phase in the argument below. If the perfect electric conductor (PEC) is adopted as the substrate, the electric field cannot penetrate into the substrate and vanishes at the interface. This results in a reflection phase $\phi_{b,PEC}$ of π , leading to a condition that $d = \lambda_0 / 4n_s$ in order to maximize absorption. If we use metals with finite dielectric constants, the electric field has a non-vanishing penetration into the metal. Consequently, the reflection phase pickup becomes larger and the required semiconductor thickness is smaller. The reflection phase pickup from a semiconductor layer to a metal with finite conductivity depends on the ratio between the amplitudes of dielectric constants in the semiconductor and metal. Figure 2(d) shows the reflection phase pickup from a layer with ϵ_1 to a hypothetical lossless metal with $\epsilon_2 = \epsilon_{2,r} + i\epsilon_{2,i}$ where $\epsilon_{2,r} < 0$ and $\epsilon_{2,i} = 0$ as a function of ϵ_2 / ϵ_1 . As the metal has smaller $|\epsilon_2|$, the reflection phase pickup increases from π (or 180°) to 2π (or 360°).

One can make a quick intuitive estimate of the magnitude of the imaginary part of the refractive index that is required to produce the maximum absorption. With the absorbed power per unit volume equaling of $Q_{Abs} = 0.5\omega\epsilon_0 \text{Im}(\epsilon)|E|^2$ and the incident power equaling $P_{Inc} = 0.5c\epsilon_0 |E_0|^2$ the absorptance is:

$$A = \int dQ_{Abs} / P_{Inc} = k_0 \text{Im}(\epsilon) \left(\int |E(z)|^2 dz \right) / |E_0|^2. \quad \text{Eq. (4)}$$

Here, $|E_0|$ is the magnitude of the incident light wave and $|E|$ is the magnitude of the electric field in the film. On resonance with a perfect electric conductor, the electric field intensity is around $|E_0|$ at the surface and zero at the conductor surface. Therefore we can estimate $\int |E|^2 dz$ in Eq. (4) to be roughly equal to $(d/2)|E_0|^2$. By putting this result into Eq. (4) as well as unity absorption ($A = 1$), we have $k_0(d/2)\text{Im}(\epsilon) = n_s k_s k_0 d \approx 1$, where k_s is the imaginary part of the refractive index of the semiconductor layer. Here the product $n_s k_0 d$ is fixed by the maximum absorption conditions

expressed in Eq. (2). With the reflection phase at Ge/Air being small, the maximum absorption condition can be rewritten as $n_S k_0 d \approx \pi - \phi_b/2$. We thus find that $k_S \approx 1/(\pi - \phi_b/2)$. For a PEC ($\phi_b = \pi$) we find $k_S \approx 2/\pi \approx 0.64$. For a “softer” metal that allows for field penetration with $|\varepsilon_s| \approx |\varepsilon_m|$ and a reflection phase $\phi_b = 1.5\pi$, $k_S \approx 4/\pi \approx 1.27$. For most common metals the required k_S for the semiconductor layer will lie between these values.

The wavelength of maximum absorption can be easily tuned by changing the semiconductor layer thickness. Figure 3(a) shows the absorption spectra (solid lines) and the classical (Yablonovich) limit (dashed lines) for the Ge layer thickness of 10 nm (red), 20 nm (green), and 30 nm (blue). The absorption peak wavelength redshifts with increasing film thickness as a longer wavelength requires a thicker cavity to stay on resonance. As the Ge layer gets thicker, the absorption peak exhibits a redshift and is reduced in magnitude, falling below the Yablonovitch limit. This is because the imaginary part of dielectric constant of Ge in this spectral range is not sufficiently high. In order to quantitatively analyze the extent of the redshift, we plot in Fig. 3(b) the absorption peak wavelength as a function of the Ge layer thickness. The slope is obtained to be around 12.5. This indicates the slight change of the Ge thickness on the order of tens of nanometers can give rise to a substantial shift of the resonance wavelength in the order of hundreds of nanometers, allowing for manipulation of the absorption band.

So far we have assumed the ideal case of perfectly planar films with uniform thickness. Practical devices may have non-uniform film thickness. To investigate the effect of such non-ideal case, we carried out calculations the absorption spectrum in the air/Ge/Ag Gires-Tournois interferometers. The thickness is assumed to exhibit the normal distribution with the mean thickness of 12 nm, which is the same as that used in the ideal case, and various standard deviations (σ). The absorption spectra for σ of 0 nm (the ideal case), 2 nm, and 4 nm, and the thickness distributions are shown in Fig. 3(c) and its inset in the red, green, and blue lines, respectively. The slight discrepancy from the ideal case is observed for the absorption spectrum for the standard deviation of 2 nm (green), indicating that the proposed configuration is robust to the thickness nonuniformity. As we increase the thickness deviation up to 4 nm (blue), the maximum absorption peak gets weaker. The absorption in the short wavelength range grows slightly. This can be ascribed to the presence of thin Ge layers. As a result of averaging effects, the short-circuit photocurrent densities are 20 mA/cm² for the thickness standard deviation of 0 nm, 2 nm, and 4 nm.

From this research it is clear that we cannot achieve unity absorption at any desired wavelength of choice when given materials (Ge and Ag) with fixed optical properties. This can be achieved using Metamaterials.

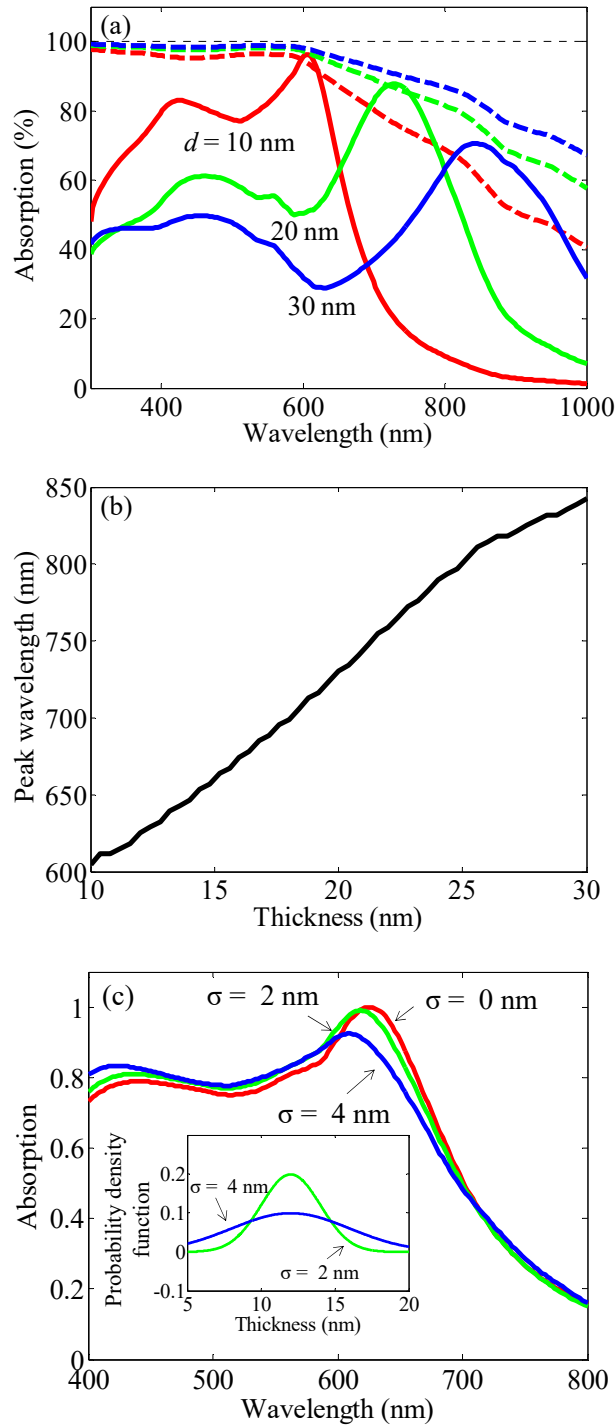


Figure 3. (a) Absorption spectrum (solid line) and Yablonoitch limit (dashed line) for the air/Ge/Ag configuration with the Ge thickness of 10 nm (red), 20 nm (green), and 30 nm (blue). (b) Absorption peak wavelength as a function of the semiconductor thickness. (c) Absorption spectrum for the air/Ge/Ag configuration with the normal distribution (shown as the inset) of the Ge thickness. The standard deviation (σ) is 0 nm (red), 2 nm (green), and 4 nm (blue), and the mean is 12 nm.

II.3. Achieving near-unity absorption in semiconductor metafilms at any wavelength

Figure 3 showed that unity absorption could not simply be obtained at any desired wavelength of illumination. It was found that unity absorption can only be attained at one wavelength for a very specific choice of the absorbing semiconductor layer thickness. This is because the optical materials properties of bulk semiconductors and metals are fixed. Next, we show that metamaterials concepts can be used to achieve near-unity light absorption at any wavelength of choice.

Above we demonstrated that the condition for strong absorption in a Gires-Tournois interferometer is related to a propagating phase inside the lossy film and a reflection phase pickup of light impinging from the lossy film on the metallic mirror. A study on the destructive interference between partially reflected waves from the Gires-Tournois interferometer revealed that unity absorption only occurs when $2nk_0t + \phi_b - \phi_t = 2m\pi$. Here, n is the refractive index of the lossy film, k_0 the free space wave number ($= 2\pi / \lambda_0$, with λ_0 the wavelength), t the lossy film thickness, ϕ_b and ϕ_t the reflection phases at the bottom and top interfaces, respectively, and m an integer indicating the order of resonance. We can deduce two approaches for tuning the wavelength that satisfies the strong absorption condition. One way is to change the thickness t ; as the lossy film becomes thicker, the wavelength that suffices the destructive interference needs to increase. This linked to the scale invariance of Maxwell's equations. However, the wavelength range in which simple geometric scaling is applicable is limited due to material dispersion that affects n and the changes in the reflection phase.

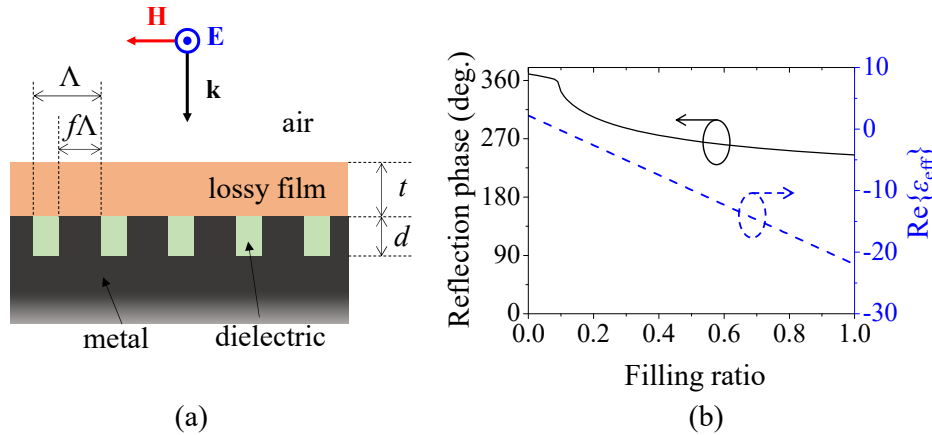


Figure 4. (a) Schematic diagram of a Gires-Tournois interferometer composed of a lossy film on a metallic metasurface (b) Reflection phase (the left y-axis) and the real part of the effective dielectric constant (the right y-axis) as a function of the filling ratio of the metallic metasurface.

The other way is to tailor the reflection phase pickup ϕ_b by changing geometrical parameters of the metallic metasurface that consists of 1-D subwavelength gratings composed of metal and dielectric material (See Fig. 4a). Fig. 4(b) shows the relationship between the reflection phase pickup (left y-axis) and the filling ratio f , which is defined as the volume fraction of the metal. We assume that the semi-infinite ($d \rightarrow \infty$) metallic metasurface is composed of silver (Ag) and polymethyl methacrylate (PMMA) with infinitely small period ($\Lambda \ll \lambda_0$). The effective dielectric

constant ϵ_{eff} (the right y -axis in Fig. 4(b)) of the metallic metasurface is obtained by invoking the Maxwell-Garnett formula⁶:

$$\epsilon_{eff} = f\epsilon_m + (1-f)\epsilon_d. \quad \text{Eq. (5)}$$

The lossy film is chosen to be copper indium gallium selenide (CIGS). At the wavelength of 600 nm, the dielectric constants of Ag, PMMA, and CIGS are $\epsilon_m = -22 + 0.32i$, $\epsilon_d = 2.2$, and $\epsilon_l = 8.7 + 2.4i$, respectively. We consider the TE case, where the electric field is parallel to the grating, as shown in Fig. 4(a).

We observe in Fig. 4(b) that the reflection phase ϕ_b is larger than 180° for the planar metallic mirror ($f = 1.0$). Here the reflection phase 180° corresponds to the reflection phase from the perfect electric conductor (PEC). Due to the finite conductivity of the metal, which is linked to the finite-valued permittivity (ϵ_m), the electric field can penetrate into the metallic mirror, resulting in a reflection phase larger than 180° . As we decrease the volume fraction of metal and increase that of dielectric, the electric field can penetrate deeper into the metallic metamaterial, giving rise to the increased reflection phase. Consequently, the real part of the effective dielectric constant changes from -22 to 2.2, as the filling ratio f is decreased from 1 to 0. This leads to a change in the reflection phase from 245° to 370° . Owing to this change in the reflection phase, it is possible to tune the wavelength that satisfies the strong absorption condition. For example it is expected that the wavelength for the destructive interference exhibits a redshift as the filling ratio decreases.

To analyze the effect of the reflection phase change, we carry out theoretical analysis of which the results are shown in Fig. 5(a). A transfer matrix method (TMM) for the anisotropic geometry is used. The materials are the same as in Fig. 5(b), and the thickness of the lossy film t is 20 nm. We assume the metallic metamaterial is semi-infinite in depth and features an infinitely small period, so that the metallic mirror itself can be modelled as a homogeneous anisotropic material (inset of Fig. 5(a)). For the planar metallic mirror ($f = 1.0$), the peak absorption occurs at a wavelength of 478 nm. As we decrease the filling ratio of the metal, the wavelength for a maximum absorption (solid white line in Fig. 5(a)) exhibits redshift. The filling ratio $f = 0.3$ features a maximum absorption wavelength at 607 nm. This spectral shift confirms the prediction above. The dashed black curve denotes the filling ratio at a certain wavelength below which the real part of the effective dielectric constants becomes positive, and thus the metallic metasurface does not play a role of mirror anymore.

Meanwhile, the Maxwell-Garnet formula in Eq.(5) is based on the assumption that the electromagnetic field distribution in each material is almost uniform, so that the optical response is homogeneous. This can be satisfied if the period of an alternatively stacked structure is very small compared to the wavelength, and the size is large enough with regard to the penetration depth of light into the metamaterial. It is thus required to implement a thick grating with a small period. However, the fabrication of such structures is limited by the pattern resolution and the achievable aspect ratios. It is necessary, therefore, to investigate the appropriate regime that results in the convergence and is also feasible in terms of fabrication.

For this purpose full-field electromagnetic simulations are performed for various periods and depths (Fig. 5(b) and the inset) by the rigorous coupled-wave analysis RCWA technique. The material combination is the same as those used in Fig. 5(a). The period is 100 nm and the depth is 60 nm. These specifications are plausible in standard fabrication technologies. It is noteworthy that the overall behavior of the absorption calculated from the full-field simulation is in good agreement well with that from the anisotropic TMM analysis. The maximum absorption wavelength (the dashed white line) exhibits a redshift as the filling ratio decreases.

In addition to a normal incidence, we also examine oblique incidence case. The red, black, and blue lines in Fig. 5(c) denote the maximum absorption wavelength as a function of the filling ratio for the incident angles of 0° , 30° , and 60° , respectively. The solid and dashed lines correspond to the results from TMM and RCWA, respectively. The absorption property is robust to the change of the incident angle. This beneficial property comes from the high refractive index of the lossy film, which leads to negligible variation in the longitudinal wavevector in the lossy film under the change of the incident angle. A more detailed discussion can be found in.

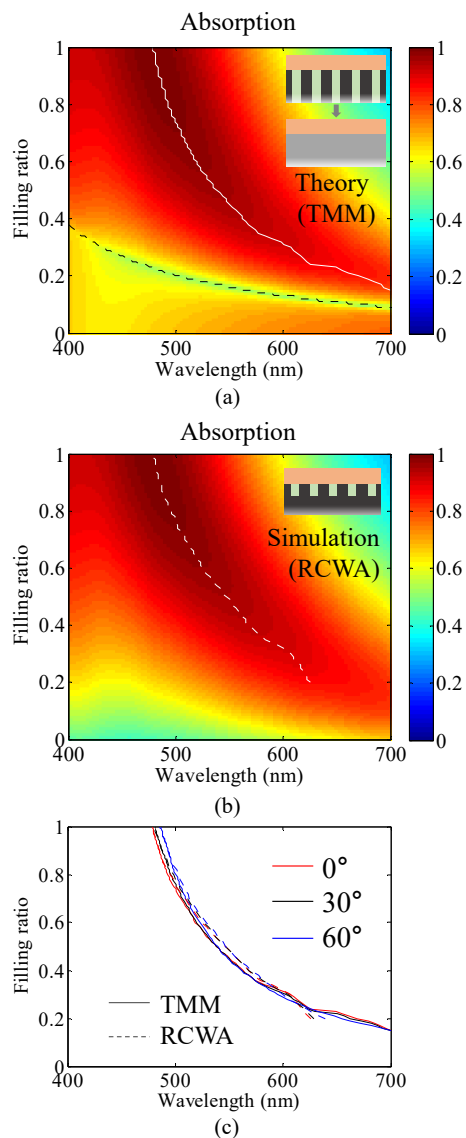


Figure 5. (a) Absorption for various wavelengths and filling ratios obtained by using the TMM while assuming a semi-infinite ($d \rightarrow \infty$) metallic metamaterial reflector and an infinitely small period ($\Lambda \ll \lambda_0$). Solid white line for the maximum absorption wavelength and the black dashed line for a regime where $\text{Re}(\epsilon_{\text{eff}}) < 0$. (b) Absorption calculated by using the RCWA technique with $d = 60$ nm and $\Lambda = 100$ nm. Dashed white line for the maximum absorption wavelength. (c) Maximum absorption wavelength as a function of the filling ratio for various incident angles of 0° (red), 30° (black), and 60° (blue), obtained by using TMM (solid) and RCWA (dashed).

Currently, we are working towards an experimental realization of the above concepts are fabricating thin semiconductor Germanium layers on top of nanostructures metal films. If successful, this approach can be of great value to achieve near-unity absorption at any desired operational wavelength across the visible range using Ge as a semiconductor).

II.4. Building blocks for superabsorbing semiconductor films

In section II.3, we demonstrated that a continuous semiconductor (Ge) layer placed on a patterned metallic (Ag) backreflector can exhibit near-unity absorption at any wavelength of interest across the visible spectrum. In this program we also proposed to demonstrate that the same can be achieved by patterning the semiconductor layer instead. To this end, we started by analyzing the basic building blocks of patterned metafilm: semiconductor nanoblocks. Such blocks can easily be created by depositing a semiconductor film and a subsequent patterning and etching step. This work was done with a former postdoc from the Brongersma group, Prof Minkyoo Seo from KAIST. He sent a postdoc to Stanford to work jointly on this project with a current postdoc: Juhung Kang.

Subwavelength nanostructures support optical resonances that facilitate highly efficient interconversion between propagating electromagnetic waves and strongly localized electromagnetic near-fields. Their outstanding ability to receive and concentrate optical radiation has been used to improve imaging techniques, sensing, heat transfer, nonlinear signal conversion, and photodetection⁷. Resonant subwavelength nanostructures are also essential as photonic artificial atoms to form metasurfaces which are ultrathin planar optical components that provide arbitrary control of the phase, amplitude, polarization, and/or wavefront of a light beam⁸. In recent decades, metallic nanostructures have been investigated intensively and used to concentrate light into deep subwavelength volumes via collective electron excitations known as surface plasmons. However, their application has been limited in extent because of the lossy nature of metals. Recently, high-refractive-index dielectric nanostructures, e.g., semiconductor nanospheres and nanowires, have been proposed as a good alternative to their metallic counterparts in many applications, owing to not only their low material losses but also their ability to support both electric and magnetic resonant modes in simple geometries.

The excitation of strong optical resonances, termed Mie or leaky-mode resonances, breaks down the stereotype that useful sizes of dielectric nanostructures have to be limited to the wavelength-scale or larger dimensions. In particular, the fundamental transverse magnetic (TM_{01}) mode, which is easily excited in semiconductor nanowires by plane wave excitation, affords a truly subwavelength-scale mode area beyond the free-space optical diffraction limit and thus allows the demonstration of vibrant structural color generation, high-performance photovoltaics, and a variety of nanoscale opto-electronic devices. However, in contrast to those of semiconductor nanowires, the detailed properties of the optical resonances in subwavelength-scale Si nanoblocks have not been thoroughly investigated yet. For example, most theoretical analyses of the leaky-mode resonances of three-dimensional nanoparticles are based on the Mie scattering theory assuming spherical or ellipsoidal shapes. To provide guidelines for engineering semiconductor nanoblocks for a desired application, rigorous and systematic research on the leaky-mode resonances in subwavelength-scale nanoblocks is required. Given the ease of fabrication of such structures using planar device fabrication technologies, this is a very worthwhile endeavor.

In this program, we theoretically and experimentally reveal the light scattering properties of Si nanoblocks that feature critical dimensions on the deep subwavelength scale. Finite-difference time-domain (FDTD) simulations and dark-field scattering microscopy are used to analyze the gradual evolution of the leaky-mode resonances of a nanoblock to those of an infinitely long nanowire. A wide spectral tunability across the

visible is demonstrated as the size is changed. We also find that different resonances exhibit different dependences of the resonant wavelengths on the length of the blocks. This can be used to spectrally align scattering resonances and to achieve very large scattering efficiencies or very strong absorption.

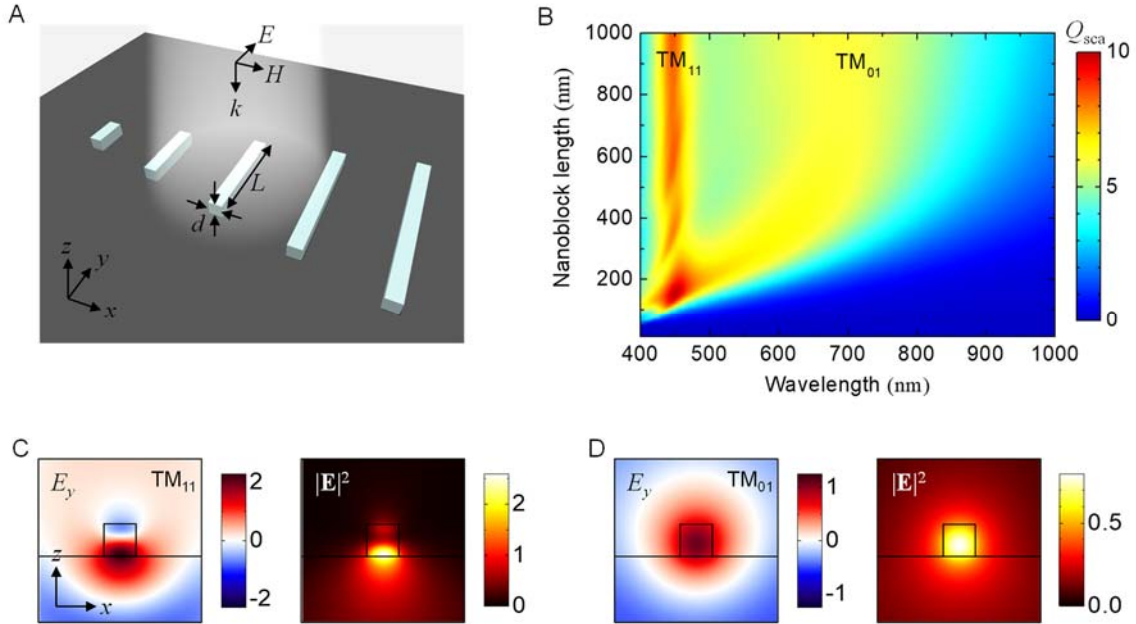


Figure 6. (A) Schematic illustration of Si nanoblocks under planewave illumination. The Si nanoblocks have a square cross section of side d and a length of L . (B) Two-dimensional map of the calculated scattering efficiency Q_{sca} of Si nanoblocks with a square cross section measuring 60 nm on a side as a function of the wavelength of light and the nanoblock length under normally incident TM-polarized planewave illumination. Profiles of the scattered electric field parallel to the nanoblock axis (left) and total intensity of the scattered electric field (right) for an infinitely long Si nanowire with a square cross section measuring 60 nm on a side at (C) TM_{11} ($\lambda = 440$ nm) and (D) TM_{01} ($\lambda = 725$ nm) mode resonances. The square cross section of the nanoblock and nanowire measures 60 nm on a side. The field and intensity magnitudes are normalized to those of the incident planewave.

The resonant modes supported by one-dimensional Si nanowires can be characterized as transverse-magnetic (TM) or transverse-electric (TE) modes similar to those in cylindrical nanowires. They can be labeled similarly by analyzing them in cylindrical coordinates. With that choice, the modes are written as TM_{ml} or TE_{ml} , where m and l are the azimuthal and radial order mode numbers, respectively. The azimuthal mode number is linked to the number of antinodes a in the dominant field that are encountered in a trajectory along the circumference of the structure ($m = a/2$). One can think of this quantity as the number of effective optical wavelengths that fit around the circumference. The radial order mode number describes the number of field maxima that are encountered along a radial direction within the structure. Under plane-wave illumination with the electric field parallel (or perpendicular) to the long axis of a nanoblock, only TM (or TE) modes can be excited for symmetry reasons. These resonances can be followed in their

evolution from those of an infinitely long nanowire to those of a finite-length nanoblock. Figure 6A shows a schematic illustration of a series of Si nanoblocks with a square cross section on a quartz substrate under normally incident planewave illumination. The total-field/scattered-field technique was employed in the FDTD simulation to realize the planewave incidence and analyze the scattering properties of the Si nanoblocks rigorously.

Figure 6B shows a two-dimensional map of the calculated scattering efficiency Q_{sca} of Si nanoblocks with a square cross section measuring 60 nm on a side as a function of the length of the nanoblock and the wavelength of the incident light. The scattering efficiency is defined as the ratio of the scattering cross section to the physical cross section of the nanoblock. When the incident planewave is polarized parallel to the long axis of a nanoblock (along the y axis), only TM resonances are excited. The Si nanoblocks exhibit two strong TM resonances in the spectral range from 400 to 1000 nm. The two resonances are derived from the TM_{01} and TM_{11} modes of an infinitely long nanowire having a cross section identical to that of the nanoblock. The TM_{11} mode has a relatively narrow spectral width, and its resonance wavelength of $\lambda_0 = 440$ nm is almost independent of the length of the nanoblock. Considering that the half-wavelength in the Si medium, $\lambda/2n_{\text{Si}}$, is ~ 50 nm and thus similar to the width of the nanoblock, it is understandable that the wavelength-scale TM_{11} mode is shifted very little by changes in the length of the nanoblock. On the other hand, the resonance wavelength for the fundamental TM_{01} mode is larger ($\lambda = 725$ nm) and the cross-sectional area is significantly smaller than the square of the half-wavelength of light in the medium, $(\lambda/2n_{\text{Si}})^2$. Note that the subwavelength-scale TM_{01} mode resonance can be widely tuned across the entire visible wavelength range from 440 to 725 nm by changing the length of the nanoblock from 150 to 650 nm. The tuning range can be extended to the near-infrared range by using wider nanoblocks.

As the length of the nanoblock increases, its resonant modes are gradually converted into the leaky resonant modes of an infinitely long nanowire.³¹ When the length of the nanoblocks exceeds 650 nm, the resonant wavelengths and spectral widths of the TM_{01} and TM_{11} modes converge to those of an infinitely long nanowire and the scattering cross section divided by the nanoblock length approaches the one-dimensional scattering cross-sectional length of the infinitely long nanowire. Figures 6C and 6D show the scattered electric field profiles of the TM_{11} ($\lambda = 440$ nm) and TM_{01} ($\lambda = 725$ nm) modes supported by the infinitely long nanowire, respectively. The TM_{11} mode, with a higher azimuthal mode number ($m = 1$), features a nodal plane in the core of the nanowire, and the electric field intensity maximum occurs near the bottom of the nanowire (Figure 6C). The asymmetry of the field profiles is due to the presence of the substrate and retardation effects. The electric field profile of the TM_{01} mode shows a single maximum near the center of the nanowire (Figure 6D). As the length of the nanoblock becomes smaller than 650 nm, the subwavelength-scale TM_{01} mode resonance rapidly blue-shifts, and it eventually spectrally overlaps the TM_{11} mode resonance when the length of the nanoblock is reduced to 150 nm. The favorable overlap of the TM_{01} and TM_{11} mode resonances enables a notably large scattering efficiency of ~ 9.95 , and the scattering cross section approaches the theoretical lowest-order single-channel scattering limit for a subwavelength-scale nanostructure. This strong scattering phenomenon based on the spectral alignment of two resonances will be discussed in detail later, together with the near- and far-field profiles of the TM_{01} and TM_{11} modes of the nanoblocks. The undulation in the magnitude of the scattering efficiency of the TM_{11} mode with changing nanoblock length in Figure 1B is

due to the presence of higher-order longitudinal Fabry–Perot (FP) resonances supported by the two reflecting end facets of the nanoblocks. Under TE-polarized illumination, only wavelength-scale TE_{01} resonances are supported at 440 nm almost independently of the length of the nanoblocks.

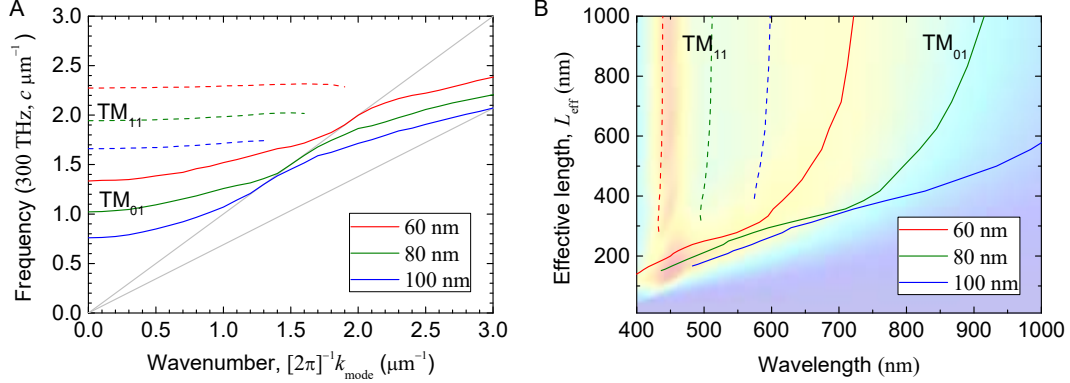


Figure 7. (A) Dispersion curves of the TM_{01} (solid) and TM_{11} (dashed) modes supported by square Si nanowires with cross-sectional widths of 60 nm (red), 80 nm (green), and 100 nm (blue) placed on a quartz substrate as a function of the wavenumber along the nanowire axis, k_{mode} . The solid gray lines represent the light lines in the air (upper) and quartz (lower), respectively. (B) Effective length of nanoblock ($L_{\text{eff}} = \pi/k_{\text{mode}}$) for the TM_{01} (solid) and TM_{11} (dashed) modes of the Si nanowires as a function of the resonance wavelength from the dispersion curves. The plots are overlaid on top of the scattering efficiency map of the Si nanoblock with a cross-sectional width of 60 nm from Figure 6B.

To understand the length dependence of the TM_{11} and TM_{01} resonances of the nanoblocks systematically, we calculated the dispersion curves of the leaky TM modes supported by the Si nanowires as a function of the wavenumber along the nanowire axis, k_{mode} , using FDTD simulations employing a broadband point electric dipole source polarized parallel to the nanowire axis (Figure 7A). The dispersion curve of the TM_{11} mode is almost flat over a large wavenumber range near the zone center until it approaches the light line, and the resonant frequency of the TM_{11} mode is almost fixed at 680 THz, corresponding to a free space wavelength of ~ 440 nm (red dotted line in Figure 2A), which is the TM_{11} mode resonant wavelength of the Si nanoblocks in Fig. 7B. On the other hand, the TM_{01} mode is dispersive, and its dispersion curve crosses the light line (red solid line in Figure 7A). As the wavenumber increases, the resonant frequency of the TM_{01} mode increases rapidly, and the slope of the dispersion curve becomes even steeper near the light line of air. The frequency at $k_{\text{mode}} = 0$ is ~ 410 THz, corresponding to a free space wavelength of ~ 725 nm, which is the resonant wavelength of the TM_{01} mode in the infinitely long nanowire. It is notable that, for a sufficiently large wavenumber, the frequency of the TM_{01} mode becomes as high as that of the TM_{11} mode. This explains the spectral overlap of the TM_{01} and TM_{11} mode resonances in a short nanoblock supporting a large wavenumber.

For quantitative analysis, we overlaid the dispersion curves of the TM_{01} and TM_{11} modes of the Si nanowires on top of the scattering efficiency map of the Si nanoblock with a cross section of 60 nm, using an FP resonance condition, $2k_{\text{mode}}L_{\text{eff}} = 2\pi$ (Figure 7B). Here, L_{eff} is the effective length of the nanoblock supporting the first longitudinal FP

resonance. In infinitely long nanowires, the planewave incident in the normal direction can only couple to the mode at $k_{\text{mode}} = 0$. But, the finite nanoblocks, due to their 3D shape that features abrupt edges, enable the normally incident light to excite the leaky-modes with any possible k value. Indeed, it clearly shows that the scattering properties and spectral behavior of the Si nanoblock can be fully understood in terms of the dispersions of the leaky TM_{11} and TM_{01} modes in the nanowire with an identical width and height. The FP resonance can be made even more accurate by taking into account a reflection phase pickup at the end of the nanoblocks, as was done for plasmonic resonators and this has been done for nanowires. The dependence of the phase pickup on the resonance wavelength causes the difference between the effective length and the actual length of the nanoblock. However, as shown in Figure 7B, the contribution of the phase pickup is not substantial for nanoblocks longer than ~ 200 nm.

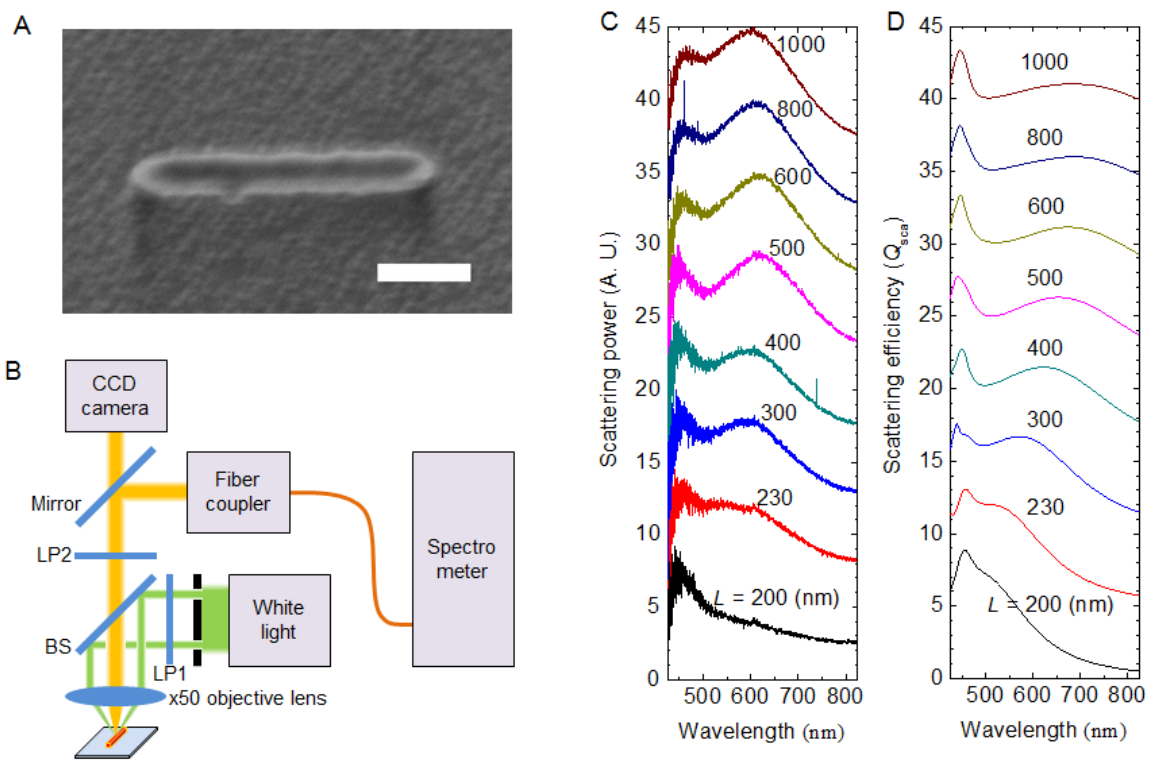


Figure 8. (A) Top-view scanning electron microscopy image of a fabricated Si nanoblock with a cross section of 60 nm on a side and a length of ~ 600 nm (scale bar: 200 nm). (B) Schematic illustration of the light scattering measurement setup based on a dark-field microscope. BS: beam splitter, LP: linear polarizer. (C) Measured scattering spectra of Si nanoblocks with different lengths. (D) Calculated scattering efficiency of Si nanoblocks with lengths corresponding to those used in the experiments. For clarity, the spectra have been displaced vertically by 5 for each additional layer.

Si nanoblocks with lengths ranging from 200 to 1000 nm were fabricated on a quartz substrate using standard semiconductor fabrication processes (see Figure 8A). Both the width and height of the fabricated nanoblocks were fixed at 60 nm. The light scattering properties of single Si nanoblocks were measured using a dark-field optical microscope

coupled to either a charge-coupled device (CCD) camera or a fiber-coupled spectrometer, as illustrated in Figure 8B. A 50× (N.A. 0.8) dark-field microscope objective was used to illuminate a single nanoblock with white light and collect the scattered signals from the nanoblock. Linear polarizers were used to control and analyze the polarization state of the incident and scattered light to characterize the TM mode resonances of the nanoblocks. As shown in Figure 8C, the measured TM₁₁ resonance remains practically fixed at ~450 nm irrespective of the nanoblock length. On the other hand, the TM₀₁ mode resonance shifts from ~600 nm to ~450 nm as the length of the nanoblock decreases from 1000 to 200 nm. Figure 8D shows the simulated total scattering efficiency for different nanoblock lengths, which agrees well with the measured scattering spectra of the leaky-mode resonances. The differences in the resonance position and scattering power between the simulated and measured spectra are due to the limited collection solid angle in the experiments and fabrication imperfection of the nanoblocks. In the experiments, only the light scattered into the objective lens with a numerical aperture of 0.8 was collected and measured under the reflected dark-field illumination condition. For example, the TM₁₁ resonance features lower backward scattering and thus shows a smaller scattering power in reflected dark-field scattering measurement than the TM₀₁ resonance.

In the next stage, we will use our knowledge of the basic scattering and absorption properties of Si nanoblocks to create super absorbing semiconductor metafilms capable of strong absorbing light at any target wavelength of interest. We will also explore the possibility of introducing random size variations to realize broadband near-unity absorption in metafilms.

II.5. Superabsorbing artificial metal films constructed from semiconductor antennas

The achievement of very strong light-matter interaction in ultrathin semiconductor layers is key to realizing next-generation optoelectronic applications. Thinner devices are more lightweight, flexible, and offer advantages in terms of reduced materials and processing cost. Shrinking device dimensions can also result in an improved performance. For example, achieving strong light absorption in increasingly thin semiconductor layers will naturally result in increases in the speed and efficiency of photocarrier extraction. This finds application in a wide variety of technologies, including solar energy harvesting⁹, photodetectors¹⁰ and thermal photovoltaics¹¹.

From the early 1900s, researchers have been eager to understand the ultimate limits to absorption of electromagnetic waves in layers of material that are much thinner than the wavelength λ of the incident radiation. Woltersdorf¹² and Salisbury¹³ explored these limits for thin metal and lossy dielectric films with and without backreflectors. Here, we aim to understand the maximum absorption one can achieve in a subwavelength layer of semiconductor material deposited on a transparent substrate. As a starting, reference point, it is of value to note that the absorption limit of an ultrathin ($t \ll \lambda$) free standing film in air is exactly 50%. Unity absorption can only be reached with the aid of back reflector.

In order to reach the 50% limit, Woltersdorff concluded that the film needs to be a metal with a purely real-valued sheet resistance of $R = \eta / 2 \approx 188.5 \Omega / \square$, where $\eta = \sqrt{\mu_0 / \epsilon_0}$ is the impedance of free space. This facilitates the best possible impedance match of a homogeneous thin film to its environment, minimizing the reflected and

transmitted power. This conclusion could have been reached by creating a map of the light absorption versus the real and imaginary parts of the relative permittivity ϵ' and ϵ'' . Figure 9(a) shows such a map for a free standing, 40-nm-thick film at the wavelength of 600 nm, in the visible range.

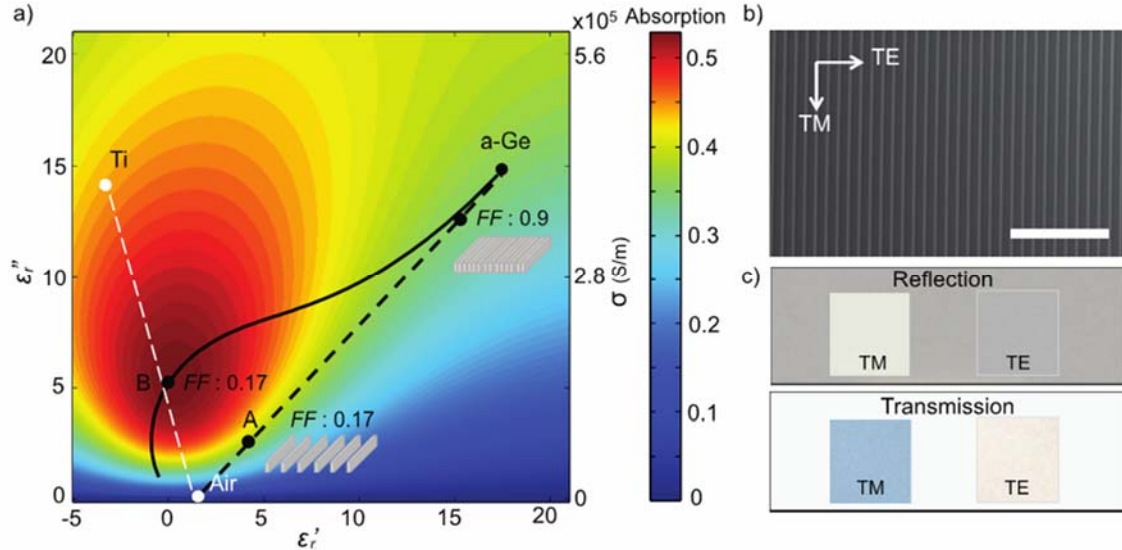


Figure 9. Optimizaton of the light absorption in a thin free-standing film. a) Absorption map of a thin, free-standing film as a function of its optical properties. The film is chosen to be 40 nm thick and the illumination wavelength is 600 nm. Dashed lines represent the achievable effective optical constants with metafilms of different compositions (white : Ti/Air, black : Ge/Air) and as obtained by first-order effective medium theory. Black solid line shows the achievable effective optical constants of a metafilm composed of 50-nm-wide, resonant Ge nanobeams and air. Point A and B are the optical constants with a Ge filling fraction of 0.17. b) SEM image of a fabricated metafilm constructed from an array of 50-nm-wide, resonant Ge nanobeams on a quartz substrate. Scalebar is 2.7 μm . c) Optical images of the white-light reflection (top) and transmission (bottom) for transverse electric (TE) and transverse magnetic (TM) polarization. The reflection and transmission of the quartz substrate can be seen in the unpatterned area surrounding the metafilm regions.

It can be observed that the maximum absorption occurs when ϵ' is small compared to ϵ'' , which happens for a relative permittivity of $\hat{\epsilon}_r = 0.436 + i5.35$. The value is slightly above 50% ($\sim 52.9\%$), which is possible due to a very small phase shift due to the propagation through the film. This is equivalent to the statement that the dielectric loss tangent, defined as the ratio of the imaginary and real part of the permittivity $\tan \delta = \epsilon''/\epsilon'$ needs to be large.

This general requirement holds true for all film thicknesses $t \ll \lambda$ and can be understood from an expression of the time-averaged power dissipation density associated with the material polarization at a certain angular frequency ω :

$$\langle P_d \rangle = \langle \mathbf{E} \cdot \partial \mathbf{D} / \partial t \rangle = 0.5 \text{Re} \left\{ -i\omega \widehat{\mathbf{D}} \cdot \widehat{\mathbf{E}}^* \right\} = 0.5 \text{Re} \left\{ -i\omega \varepsilon_0 (\varepsilon' + i\varepsilon'') \widehat{\mathbf{E}} \cdot \widehat{\mathbf{E}}^* \right\} = 0.5\omega \varepsilon_0 \varepsilon'' |\widehat{\mathbf{E}}|^2 \tan \delta, \text{ Eq. (6)}$$

where boldface denotes a vector quantity and the ^ symbol denotes a complex quantity. In this expression and for the rest of the paper, an $e^{-i\omega t}$ time-harmonic dependence was assumed. The dissipation is governed by the dot product of the electric field \mathbf{E} and displacement current density $\partial \mathbf{D} / \partial t$, much like the Ohmic dissipation in metals is linked to the dot product of the electric field and the current density of mobile charges $\langle P_d \rangle = \langle \mathbf{E} \cdot \mathbf{J} \rangle$. The magnitude of δ is a phase angle that quantifies how much the electric displacement lags the driving electric field: $\widehat{\mathbf{D}} = \varepsilon_0 (\varepsilon' + i\varepsilon'') \widehat{\mathbf{E}} = \varepsilon_0 |\varepsilon| e^{i\delta} \widehat{\mathbf{E}}$. From this brief analysis, the critical role δ plays in determining the optical loss is clear. The highest dissipation occurs when $\delta = 90^\circ$ and the displacement current is in phase with the electric field. For this value of δ , the oscillating current produces a scattered wave with a field that is perfectly out of phase with the field of the transmitted wave, facilitating its best possible cancelation of the forward wave. The strength of the dissipation in a lossy dielectric and conventional metal can quantitatively be compared by realizing that $\varepsilon'' = \sigma / \omega \varepsilon_0$, which links the ability to drive displacement and real currents. It is thus clear that the requirement for a real-valued sheet resistance of a metal is equivalent to the requirement for a high loss tangent in a dielectric.

The next, important question to address is how a high loss tangent can be reached with semiconductors. Typical semiconductors, such as germanium in our example, have high values of both ε' and ε'' (see Fig. 9a) and this precludes good impedance matching with a homogenous semiconductor film. In the hopes to change the situation one can leverage metamaterials, artificially-designed materials whose optical properties can be tuned by nanostructuring. We start by considering a very simple metamaterial design consisting of a dense array of deep-subwavelength nanobeams. Normally-incident light can be classified as a transverse magnetic (TM) excitation with the electric field along the nanobeams or a transverse electric (TE) excitation with the electric field in the orthogonal direction. For TM polarization the effective permittivity is simply determined by the optical properties of the two constituent materials ($\hat{\varepsilon}_1$ and $\hat{\varepsilon}_2$) and their relative filling fraction (f_1 and $f_2 = 1 - f_1$) as: $\hat{\varepsilon}_{eff} = f_1 \hat{\varepsilon}_1 + (1 - f_1) \hat{\varepsilon}_2$. Within this approximation that is valid when the structural dimensions are much smaller than the wavelength of light, the absolute size of the beams is irrelevant. Metals naturally feature a large conductivity and loss tangent. For this reason it is straightforward to design a strongly absorbing metafilm with metal beams surrounded by air. As an example, the white dashed line in Fig 9a displays the achievable effective permittivities for varying filling fractions of a 40-nm-thick titanium (Ti) metafilm, created by removing metal to create a periodic, deep-subwavelength beam array. The thickness of 40 nm was chosen somewhat arbitrarily as one that is very thin compared to the freespace wavelength of light in the visible spectral range (400 nm – 700 nm). However, the following analysis could be made for any film with a deep subwavelength thickness. A filling fraction of 0.34 metal and 0.66 air results in a permittivity approximately equal to the targeted relative permittivity value for which the absorption is maximized. Several works have demonstrated the ultimate absorption limit of 50% with nanostructured metallic

films. Furthermore, near-unity absorption has been attained with a back reflector behind the absorbing layer. Both the real and imaginary parts of the permittivity of semiconductors, on the other hand, are positive in nature and the desired optical properties for maximum absorption cannot be reached. As an example, the black dashed line depicts the achievable effective permittivities for a 40-nm-thick (same as before) metafilm constructed from an array of Ge beams with deep subwavelength dimensions. At no Ge filling fraction is 50% absorption reached. Therefore, it seems to be impossible to make the Ge-air structure act as a metallic film with a large loss tangent. Interestingly, the reverse case has been demonstrated and researched extensively. Here, a thin metal film was patterned at a subwavelength scale to make it optically look like an artificial dielectric with a high-magnitude and real-valued permittivity. As such, one may wonder whether a judiciously nanopatterned semiconductor film can be made to act optically as a thin metal layer.

Next, we demonstrate that Ge metafilms constructed from properly designed nanobeams that support optical resonances can in fact behave like metals and reach the 50% absorption limit. High-index semiconductor nanobeams with sizes as small as 10 nm and different cross-sectional shapes can exhibit Mie-like optical resonances by which light is trapped and concentrated inside the nanostructure. The first-order effective medium theory is incapable of taking into account the impact of such optical resonances on the effective optical properties. The redistribution of the fields resulting from the excitation of resonant modes requires full-field simulations or higher-order effective medium theories. The effective optical properties of a nanostructured film can be extracted from full-field simulations using standard procedures in which the transmission and reflection properties of the film are quantified. By comparing results from the first-order theory and full-field simulations, the impact of resonances on the optical properties can be analyzed. For example, the achievable effective permittivities for a 40-nm-thick metafilm constructed from an array of 50-nm-wide Ge nanobeams follow the black solid line in Fig.9a. This trajectory of achievable permittivity values deviates significantly from the linear trajectory for the metafilm constructed from very deep-subwavelength building blocks (for which the lowest-order effective medium theory holds) and moves right through the center of the high absorption region. At a filling fraction of 0.17 (point B), the loss tangent is very high ($\tan \delta = 520$) and the film optically performs very similar to an ideal conductor with the optimal conductivity of $\sigma = 1.4 \cdot 10^5$ S/m. At this point the absorption limit of 50% is reached. Figure 9b shows a scanning electron microscopy (SEM) image of such a metafilm on a quartz substrate as patterned by electron beam lithography.

Figure 9c shows optical reflection and transmission images taken from fabricated sample of a Ge metafilm with its geometrical parameters chosen as above to maximize absorption at a wavelength of 600 nm. It shows two square regions in which the Ge beams are oriented in two orthogonal directions such that the polarization of the illumination is effectively in the TM (left panel) or TE direction (right panel). The background shows the reflection from the quartz substrate that features a very high, near-unity transmission of $\sim 92\%$. The appearance of the resonant metafilm under TM illumination is much brighter in reflection and darker in transmission due to the strong, resonant light-matter interaction in the nanobeams that make up the metafilm. On the other hand, under TE illumination the film and surroundings appear similar. This results from the fact that the 50-nm-wide beams are too small to support a resonant mode in the visible spectral range for this polarization.

For this reason, the effective optical properties of the film nicely follow the first order effective medium theory and an index $\hat{n} = 1.09 + 0.003i$ close to that of air is found from simulations.

To better understand the difference between metafilms made from resonant and non-resonant building blocks, we investigate how the effective optical properties evolve as the widths of the constituent Ge beams are gradually increased. In Fig. 10 we analyze this evolution again at the illumination wavelength of 600 nm and a film thickness of 40 nm surrounded by air on both sides. We keep the Ge filling fraction fixed to 0.17, implying that an increase in the beam width comes with an increase in the period. By using a fixed filling fraction, we can directly quantify how the resonance impacts the optical properties, as for a non-resonant system the complex permittivity values would remain constant at a fixed filling fraction. Whereas the effective permittivity based on first order effective medium theory remains constant at $\hat{\epsilon}_{eff} = 3.7 + 2.4i$ (dashed lines), the extracted parameters from full-field simulations show an evolution as depicted by the solid lines in Fig. 10a. For very narrow beam widths, the permittivity extracted from full-field simulations converges to the values obtained from the first-order effective medium theory. However, as the beam width is increased, the impact of the resonance is to reduce the real part of the relative permittivity (blue), ultimately causing its magnitude to drop below zero at a width of 50 nm. At the same time, the imaginary part of the permittivity is increased, reaching a maximum value near this same width. At this width the beams are on resonance at the considered wavelength of 600 nm. For larger widths the complex permittivity values further evolve as one moves beyond the resonance. The graph is cut off for larger widths as these have corresponding magnitudes of the period at which diffracted orders are produced in the glass substrate and a metamaterials picture becomes untenable.

The presence of optical resonances in the nanobeams can also be seen in the optical electric field profile and the stream lines of the power flow (Poynting vector field) for a TM light wave that is normally-incident on a metafilm. Figure 10b shows these quantities for three representative metafilms with beam widths of 10 nm, 50 nm and 80 nm. When the beam widths are 10 nm, they are too small to support an optical resonance and most of light flows through the film undisturbed, i.e. without altering its direction. For the case of 50-nm-wide beams, the beams are on resonance and the incident light is effectively funneled into the beams due to an optical antenna effect³⁴. The 80 nm beams are too wide to be on resonance and a significant amount of light again flows past the nanobeams.

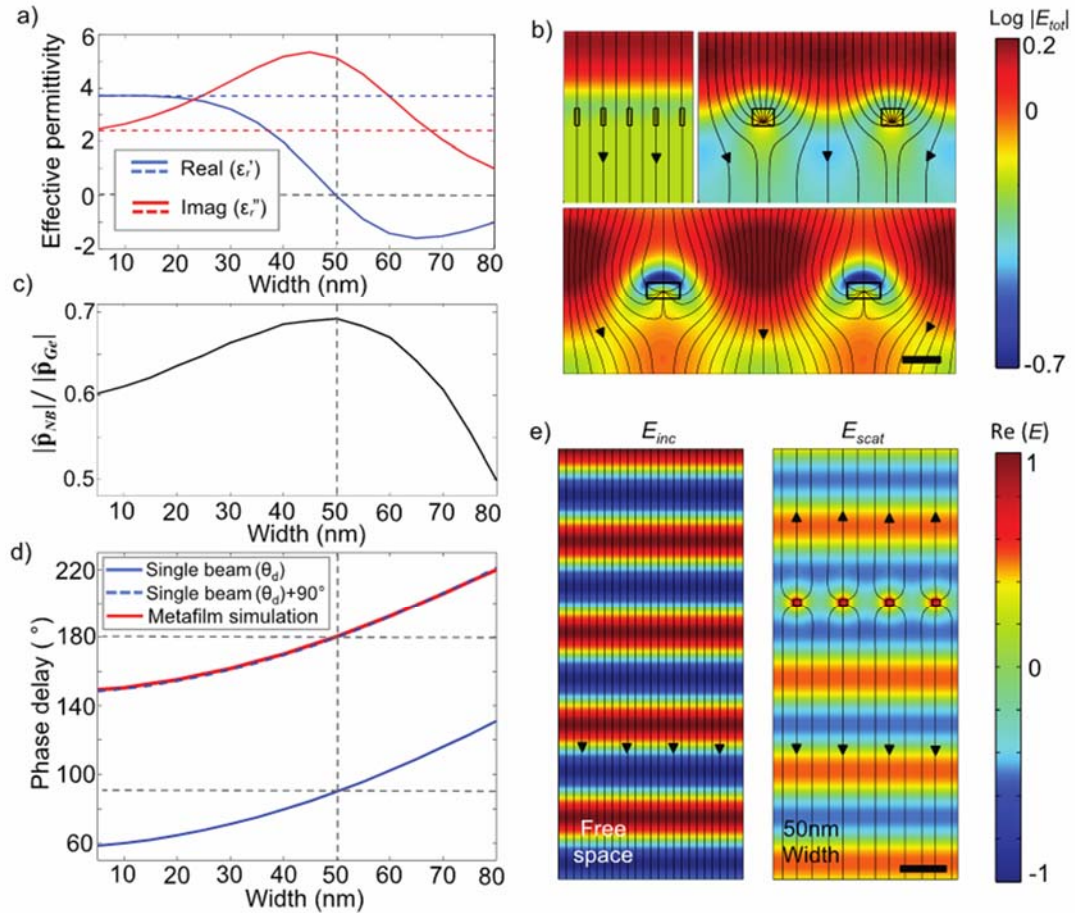


Figure 10. Evolution of the optical properties of a semiconductor metafilm from semiconductor-like to metal-like. a) Changes in the effective optical properties of a 40-nm-thick Ge metafilm upon changing the width of the constituent nanobeams. The probe wavelength was chosen to be 600 nm and the filling fraction of Ge beam-material was fixed at 0.17. The blue and red lines represent the real and imaginary parts of the permittivity. Dashed blue and red line represent the values of effective index based on first order effective medium theory. b) Maps of the total field distributions and power flow for top-illuminated metafilms with Ge nanobeams of 10 nm width (upper left), 50 nm width (top right), and 80 nm width (bottom). Scalebar for these images is 80 nm. c) Magnitude of the dipole moment of a resonant nanobeam versus the beam width. The dipole moment of the beam is normalized by the magnitude of the dipole moment the Ge beam were to have if it were polarized by the incident field. d) Changes in the phase delay of the forward-scattered wave with respect to the incident wave upon changing the Ge beam width. The case for a single beam (blue line), an estimate for an array of beams from individual beam properties (blue dotted line), and full field simulation (red) are shown. e) Maps of the incident and scattered field profiles for a top-illuminated metafilm with 50-nm-wide nanobeams. Scalebar is 300 nm.

Figure 10c and 2d analyze how the effective optical properties of the homogenized Ge metafilm emerge from the optical properties of the constituent nanobeams. These figures

show the amplitude and phase of the scattered field of the individual beams in the metafilm. Figure 10b illustrates how the resonant excitation of the nanobeams under TM polarization can produce a very simple electric field distribution with one anti-node inside the nanobeam. This field induces a displacement current along the direction of the driving electric field. The current in turn produces a scattered field that mimics that of a linear electric dipole in the far-field. As such, the beams can be treated as electrical dipole resonators with a complex polarizability $\hat{\alpha}_{NB} = |\hat{\alpha}_{NB}|e^{i\theta_d}$, where θ_d is the phase lag between the electric dipole moment created in the wire and the electric field that excites it. The dipole moment of the nanobeam can be evaluated from the full-field simulations as shown in Fig. 2b by integrating the polarization vector of the nanobeam volume V_{NB} as: $\hat{\mathbf{p}}_{NB} = \int_{NB} \hat{\mathbf{P}}(\mathbf{r}') d\mathbf{r}' = \epsilon_0 \hat{\chi}_{Ge} \int_{NB} \hat{\mathbf{E}}(\mathbf{r}') d\mathbf{r}'$ where $\hat{\chi}_{Ge}$ is the susceptibility of Ge. To get a sense for how the resonance impacts the magnitude of this dipole moment, we normalize this quantity by another dipole moment $\hat{\mathbf{p}}_{Ge} = \epsilon_0 \hat{\chi}_{Ge} \hat{\mathbf{E}}_{Inc} V_{NB}$. This is the dipole moment that would be achieved if the Ge nanobeam were polarized by the (non-resonantly enhanced) incident field $\hat{\mathbf{E}}_{Inc}$ illuminating the nanobeam. Figure 10c shows that the magnitude of the dipole moment reaches a maximum for a beam width of 50 nm. At this wavelength, the beams of this width are driven on resonance. Interestingly, the magnitude of the dipole moment does not increase very much by virtue of having a resonance in the beam. We can thus make the important observation that for highly polarizable materials such as Ge, it is not critical to use a resonance to boost the magnitude of the dipole moment to achieve strong absorption³⁵. Instead, we will show that the critical role of the resonance is to delay the scattered waves with respect to the incident wave.

The solid blue line in Fig. 10d shows that the phase of the scattered field also progresses as the width of the nanobeams is increased from below to above the resonant beam width. On resonance, the scattered fields feature a phase lag of exactly 90°. This is in agreement with the famous Lorentz (i.e. mass-spring) model for optical resonators, which teaches us that the phase lag progresses from 0 to 180° in moving spectrally through a resonance. This is related to the fact that at low frequencies the displacement of the bound charges can follow the driving fields and at frequencies above the resonance frequency they lose this ability. The non-zero phase lag at very small beam widths is related to the finite height (40 nm) of the nanobeams.

For the metafilm, the scattered waves generated by each of the individual nanobeam-resonators interfere to produce a forward-scattered wave on the transmission side. The coherent addition of the scattered fields from all of the individual beams in the plane of the film produce a forward-scattered wave with a 90° phase lag relative to the scattered field emerging from the individual beams³⁵. In the direction of propagation, the forward-scattered wave and the incident wave combine to produce the transmitted wave with a total field^{36,37}:

$$\hat{\mathbf{E}}_{tot} = \hat{\mathbf{E}}_{inc} + |\hat{\mathbf{E}}_{scat}| \cdot e^{i \cdot \theta_{film}}, \text{ where } \theta_{film} = \theta_d + \frac{\pi}{2} = \tan^{-1} \frac{\alpha_{NB}''}{\alpha_{NB}'} + \frac{\pi}{2} \quad \text{Eq.(7)}$$

Here, $\hat{\mathbf{E}}_{scat}$ is the field of the forward-scattered waves, θ_{film} denotes the phase delay of the field of the forward-scattered wave. The blue dotted line in Fig. 10d shows the progression of θ_{film} as calculated by adding $\pi/2$ to the phase calculated for the individual nanobeam resonators in the film. The red line is the phase delay for the metafilm as calculated by full-

field simulations. The red and blue dotted lines show a good quantitative agreement. It is thus clear that knowledge of the resonant properties of the individual beam can be very helpful for the design of a resonant metafilm and understanding its operation. The effective permittivities at 600 nm for the metafilms with 10 nm and 50 nm beams correspond to the points A and B in Fig. 9a. The evolutionary resonant curve in Fig 10a shows how the permittivity is transformed from A to B. The loss angle δ ($= \tan^{-1}[\epsilon''/\epsilon']$) changes from approximately 39° to 90° in going from point A to B. It can be seen that moving from non-resonant to resonant beams can be thought of as a rotation in the complex permittivity plane.

Figure 10e visualizes the phase delay of the scattered optical field for the beam width of 50 nm by making a comparison to the incident field, which serves as a useful reference. As the nanobeam width is increased from 10 nm, the scattered waves reradiated from the array are increasingly delayed with respect to the incident wave. For the width of 50 nm, the phase of the forward-scattered wave is exactly π delayed and the magnitude of the field of the forward-scattered wave equals half of the magnitude of incident field. At this optimal condition, the forward-scattered wave achieves the maximum possible destructive interference with the incident wave on the transmission side of the metafilm. At this point, 25% of the light is transmitted and 25% is reflected. This situation is exactly the same as the case of a metallic thin film with an optimized conductivity

Next, we experimentally demonstrate the above concepts with the help of reflectivity and transmissivity measurements on a judiciously designed metafilm constructed from resonant building blocks. By lithographic means, a series of 40-nm-thick metafilms with 50-nm-wide Ge beams were patterned on a quartz (c-SiO₂) substrate (see Method for fabrication steps). The array periods were varied from 500 nm to 250 nm. The array period is a critical parameter as it controls whether 1st order diffraction can occur in the SiO₂ substrate or not. The occurrence of diffracted orders by definition precludes a description of the array as a metamaterial with homogenized optical properties. This point is illustrated in Fig. 11a, which shows a schematic of the nanobeam array on a quartz substrate with the reflected and possible transmitted channel of interests. For periods that are subwavelength ($P < \lambda/n_{\text{SiO}_2}$), only the 0th-order propagates on the transmission and reflection sides. On the other hand, for periods larger than the wavelength of light in the substrate, higher-order diffraction channels open up by which the light can leave the film surface. Whereas the simulated optical field for an illumination wavelength of 600 nm and a 500 nm period show diffraction into three different orders (Fig. 11b), for 300 nm periods only the 0th order is transmitted (Fig. 11c). In the latter case, a description of the metafilm in terms of effective optical properties can be helpful. In this regime one can also conveniently estimate the absorptivity A in the film through measurements of the films reflectivity R and transmissivity T_0 into the zeroth-order as $A = 1 - R - T_0$.

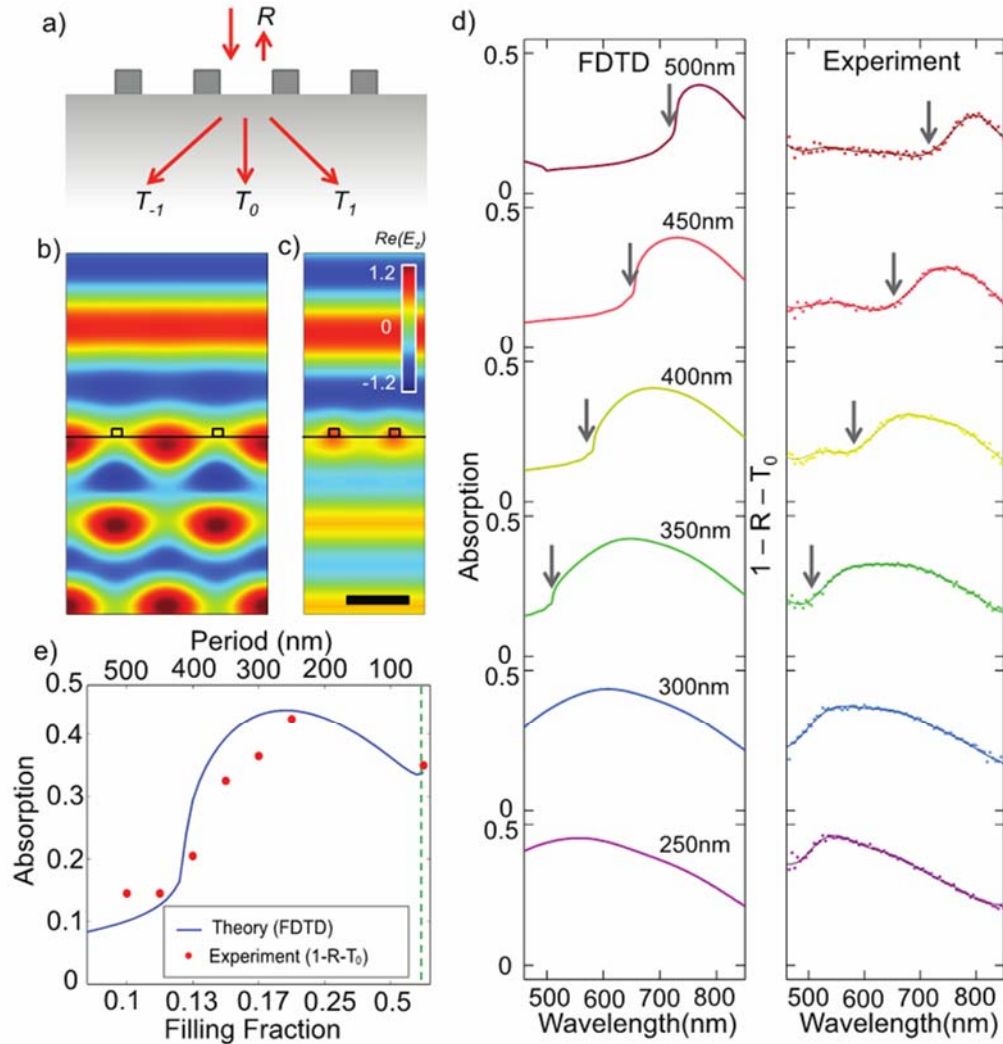


Figure 11. Experimental and simulated estimates of the absorption by designer Ge metafilms. a) Schematic of a top-illuminated Ge metafilm on a quartz substrate showing the possible reflected and transmitted channel of interests. b,c) Optical electric field profile at an illumination wavelength of $\lambda = 600$ nm and for the beam periods of 500 nm (b) and 300 nm (c). Scalebar is 300 nm. d) Simulated (left panel) and experimental (right panel) absorption spectra of the fabricated Ge metafilms with different periods labeled from 500 nm to 250 nm from top to bottom. The vertical arrows indicate the spectral locations at which $\lambda/n_{\text{SiO}_2} = P$, where the first diffraction-order channels open up in transmission. e) Absorption at $\lambda = 600$ nm in the Ge metafilms with different filling fractions/periodicities as extracted from in panel (d). The blue line provides the simulated absorption and the red dots provide experimental values of the absorption as estimated from reflectivity and transmissivity measurements as $A = 1 - R - T_0$. The vertical green dashed line indicates the period/filling fraction for a continuous film.

The left panel in Fig. 11d shows simulated absorption spectra for 6 arrays with distinct periodicities. The vertical arrows indicate the wavelength at which $\lambda/n_{\text{SiO}_2} = P$, marking the onset of first-order diffraction. It can be seen that the absorption is highest in the metamaterials regime (to the right of the vertical arrows), where higher-order diffraction channels are shut off. The right panel in Fig. 11d shows spectra of the estimated absorption, as extracted from the reflection and transmission measurements as: $A = 1 - R - T_0$. Good qualitative and quantitative agreement is obtained. The higher estimated absorption seen in the measurements on the short wavelength side of the spectrum where $\lambda/n_{\text{SiO}_2} < P$ is linked to some energy loss to light that is redirected in first-order diffracted beams that are not captured by the detector on the transmission side. The simulated absorption quantifies the actual absorption loss inside the film. Minor differences between experiments and simulations are also coming from the not-perfectly rectangular shape of the Ge beams in the experiments. Figure 11e shows the simulated and estimated absorption at the target wavelength of 600 nm, as extracted from the spectra in 11d. For periods larger than 420 nm, the absorption is low ($\sim 10\%$) due to energy loss into diffracted orders. As the period decreases into subwavelength range, the absorption rapidly increases with increasing filling fraction of Ge. This is expected as we increase the linear density of absorbing beams. For periods of 250 nm to 300 nm, the effective index approaches to the point of optimal impedance matching and the absorption reaches a maximum close to 50%. It is important to realize that the theoretical maximum absorption for a subwavelength film placed on a quartz substrate is 46.4%, which is lower than for the case of a free-standing metafilm due to the asymmetry in the index of the sub- and superstrates. Because of this fact, the magnitude of the maximum absorption found in the experiment also ends up being a bit lower (43%) than expected from the theory for a free-standing film. Ultimately, the absorption comes down for very small periods where the resonant modes from neighboring beams exhibits a very large degree of overlap and the individual beam resonances disappear. Here the absorption spectrum converges to that of a continuous Ge thin film.

With the demonstrated ability of using optical resonances in high-index nanostructures to tune the effective optical properties of a metafilm, it is worth asking the question what range of optical properties may be achievable. The larger the range of optical properties one can achieve with a single semiconductor material, the greater the flexibility in the design of specific optical functions. Figure 12 shows a map of the effective permittivities at 600 nm that are achievable by subwavelength patterning of a 40-nm-thick semiconductor. By controlling the period and width of the Ge beams, a wide range of permittivity values can be realized. To gain further insight into the way the complex-valued permittivity can be manipulated, we first analyze the evolution of this quantity as we increase the density of beams for different fixed beam widths. Each solid line represents a beam width in the range from 10 nm to 90 nm. The boundary of this set of curves indicates the range of achievable permittivities. For the smallest widths, the beams do not support a resonance and an increase in the density causes the permittivity of the metafilm to approach the permittivity of a continuous Ge film along a straight line. This directly follows from first-order effective medium theory. For wider beams that support an electrical dipole resonance (i.e. about 50 nm width), it is the imaginary part of the permittivity that primarily increases as the beams are brought close together. The real part of the permittivity stays small. This can be understood by realizing that on/near resonance, the beams feature a dipolar polarizability $\hat{\alpha}_{NB} = |\hat{\alpha}_{NB}|e^{i\theta_d}$ with a phase delay $\theta_d \approx 90^\circ$, i.e. $\hat{\alpha}_{NB}$ is imaginary.

At low density the metafilm's susceptibility is expected to follow in a simple way from the beam's polarizability and the filling fraction of Ge beam-material in a repeating unit cell f_{Ge} as: $\hat{\chi} = f_{Ge} \hat{\alpha}_{NB} / \epsilon_0$. With an imaginary $\hat{\alpha}_{NB}$, one thus expects that the imaginary part of the susceptibility and permittivity will primarily increase with an increasing filling fraction of germanium beam material. As the density of the beams is increased further, the near-field coupling between neighboring beams will increase and ultimately becomes so large that the individual beam resonances disappear. As a result the permittivity will start converging towards that of a continuous Ge film. For beams that are substantially wider than 50 nm, the real part of the permittivity can even achieve negative values.

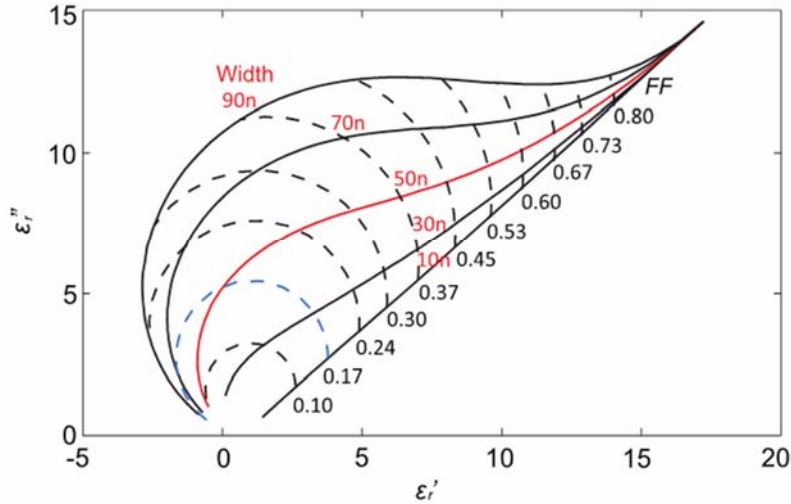


Figure 12. Range of achievable effective optical constants from Ge metafilms. Theoretical boundaries for the effective permittivities at $\lambda = 600$ nm as achievable with resonant and non-resonant Ge nanobeams with a 40 nm height. By varying either the filling fraction at a constant beam width (solid lines) or the beam width at a constant filling fraction (dashed line), a wide range of complex permittivity values can be achieved. The relevant beam widths in nanometer and filling fractions are labeled along the solid and dashed lines. The beam width and filling fraction at which the absorption of a 40-nm-thick Ge metafilm are maximized are highlighted in red and blue colors.

The dashed lines in Fig. 12 indicate the achievable permittivities that can be obtained by varying the geometrical parameters in a different way; They show the evolution in the effective permittivity of the metafilm as the beam width is varied at a constant filling fraction. At each filling fraction, the increase in beam width causes a rotation in the complex permittivity plane. The blue dashed line at a filling fraction of 0.17 shows the evolution of the permittivity for the beam-array that was discussed in Fig. 10. Consistent with Fig. 10a, the imaginary part of the permittivity increases upon approaching the beam resonance and then decreases again. At the same time the real part of the permittivity crosses zero. Figure 12 shows that these changes result in a more-or-less circular path in the complex permittivity plane and an increase in the control of loss angle.

To summarize, we have demonstrated that the ultimate absorption limit for a subwavelength thickness film can be achieved using a semiconductor metafilm.

Judiciously designed building blocks, which support optical resonances, can transform the optical properties of a metafilm from that of a semiconductor to an ideal metallic conductor. The key role of the optical resonances is to cause a delay in the phase of the scattered wave from the metafilm. The manipulation of optical resonances enables one to achieve the ultimate absorption limit in a freestanding film as originally predicted for a metal by Wilhelm Woltersdorff. The general thinking in this paper can also be used to understand the very strong absorption (even strong per unit volume) in deep subwavelength metallic nanostructures. It can also be extended to nanostructured metamaterials supporting both electric and magnetic resonances. For such materials it was recently suggested that unity absorption can be achieved in an optically thin film. For all of such films a careful optimization of the scattering amplitude and phase is required to achieve high absorption. More generally, the described metafilm design procedure can be applied to any high index material and enables one to widely tune the optical properties for a material of interest. This notion breaks open conventional design principles for optoelectronic devices which typically assume that the optical properties of semiconductor materials are intrinsic and fixed.

II.6 Anti-Hermitian Photodetector Facilitating Efficient Subwavelength Photon-sorting

The spectral separation of photons has been demonstrated using a variety of nanometallic and semiconductor nanostructures and inverse design was successfully employed to realize compact wavelength division (de)multiplexing systems. Even the splitting of optical signals at the subwavelength-scale and local enhancement of light absorption has been achieved using closely-spaced resonant plasmonic elements and metasurfaces. However, the application of subwavelength photon sorting in photodetection systems with a narrow spectral bandwidth has remained elusive. The key reasons for this are associated with practical challenges in connecting closely-spaced resonant photodetector elements and fundamental limitations in the quality factor/linewidth of subwavelength resonant optical structures that limit spectral resolution. As part of this program, we have demonstrated the possibility to spectrally sort and detect photons with a spectral separation of just 30 nm and below the diffraction limit. This is accomplished by suppressing the near-field interaction and maximizing the far-field interactions between closely-spaced photodetector elements. We illustrate how this can be achieved by capitalizing on insights derived from the physics of anti-Hermitian coupling seen in open quantum systems.

The proposed device is schematically illustrated in Fig. 13a. It shows a binary grating composed of 60-nm-wide and 80-nm-wide polycrystalline-silicon (poly-Si) nanobeams that are entrenched in a silver (Ag) film. The beams are spaced at a deep subwavelength pitch, which avoids the formation of first-order diffracted beams upon top-illumination with visible light. As such, the beam-array can be treated as a metafilm whose optical properties have been altered from a bulk semiconductor film. A thin, electrically-insulating aluminum oxide (Al_2O_3) layer separates the Si beams from the Ag film to facilitate effective extraction of photocurrent upon top-illumination. Current can be extracted separately from the sets of wide and narrow beams so that possible differences in their spectral responsivity can be explored.

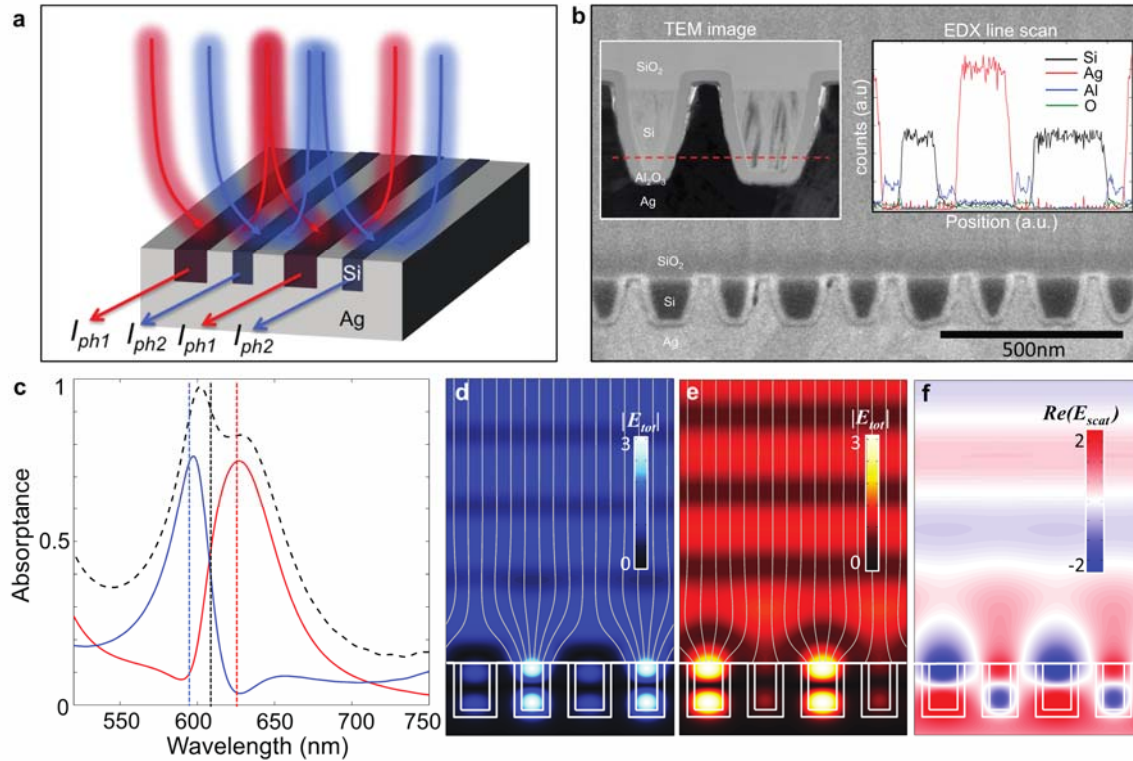


Fig 13. Fabrication and operation principle of a photon-sorting, metamaterial device that leverages anti-Hermitian coupling. (a) Schematic view of an anti-Hermitian metamaterial composed of differently-sized semiconductor nanobeams (red and blue). The geometric properties of the nanobeams are chosen to elicit an anti-Hermitian coupling that facilitates sorting of incident photons by wavelength and subsequent photocurrent extraction. (b) Cross-sectional SEM image of a fabricated device structure. Left inset shows the TEM image of a repeating unit cell of the metamaterial with electrically-insulated Si beams (light) embedded in an Ag film (dark). Right inset shows an EDX line scan along the red dashed line in the TEM image. (c) Simulated absorption spectrums of anti-Hermitian coupled metamaterial under TM-polarized illumination with the electric field oriented along the nanobeam axes. The simulated absorption spectrums for the 80-nm-wide (blue curve) and 60-nm-wide nanobeams (red curve) show how the device efficiently sorts photons with a narrow spectral separation of 30 nm. The total absorption in Si material (black dashed line) reaches a near-unity value. Three vertical lines indicate wavelengths of interests at which electric field maps are shown in panel d (blue line), e (red line), and f (black line). (d, e) Simulated images of total electric field with superposed power flow lines at the wavelengths of 595 nm (d) and 625 nm (e) showing that Mie-like resonances are excited selectively in narrow/wide beams at shorter/longer illumination wavelengths. (f) Simulated image of scattered electric field at the wavelength of 605 nm showing that the differently-sized beams scatter light with a π phase difference.

Figure 13b show a cross-sectional scanning electron microscopy (SEM) image of a fabricated device. The bi-grating is lithographically defined on a silicon dioxide (SiO₂) substrate followed by the deposition of a 17-nm-thick layer of aluminum oxide (Al₂O₃) by atomic layer deposition. Finally, an optically thick Ag film is deposited on top of the grating. In the experiments, the metamaterial is illuminated through the SiO₂ substrate. The left-inset shows a cross-sectional transmission electron microscopy (TEM) image of one repeating unit cell, showing both a narrow and a wide Si beam. We also performed energy

dispersive X-ray spectroscopy (EDX) along the red dashed line of the TEM image as seen in the right inset. The line-scan confirms the presence of a conformally-grown Al_2O_3 layer capable of electrically separating the Si nanobeams from each other and from the Ag.

Figure 13c shows the simulated absorption spectrums of the metafilm under illumination with transverse magnetic (TM) polarized light, with the electric field oriented along the nanobeam axes. The blue spectrum shows the fraction of absorbed light in the narrow beams and the red spectrum shows the same for the wide beams. From the spectrums, it is clear that 595-nm-wavelength light is most effectively absorbed by the narrow beams and 625-nm-wavelength light is more strongly absorbed in the wide beams. The sum of the absorption in the narrow and wide beams reaches a near-unity value, as shown by the black spectrum. This is useful absorption in the semiconductor that leads to the generation of photocurrent. It is noteworthy that such strong absorption can be achieved in the presence of lossy metals, which tend to cause undesired dissipation. The low losses in the metal are in part due to the fact that the subwavelength grating cannot launch propagating surface plasmon polaritons on the device surface for this polarization.

More intriguing than the very strong overall absorption is the fact that the narrow beams can absorb approximately 75 % of the incident 595 nm light, even though these beams represent just 19 % of total surface area. This implies that the absorption cross section σ_{abs} of each narrow beam under normal-incidence illumination reaches a value that is about four times larger than the geometric cross section σ_{geo} , i.e. an absorption efficiency $\eta_{\text{abs}} = \sigma_{\text{abs}} / \sigma_{\text{geo}} \approx 4$. Figure 13d shows how this is physically possible by analyzing the flowlines of the Poynting vector. It shows how normally-incident light can preferentially be funneled into the narrow beams that feature a Mie-like optical resonance with two anti-nodes located in the core of the nanobeams. Note that such resonances are distinct from plasmonic slit resonances, which can be excited when the light is polarized orthogonal to the length of the slit and feature their highest field at the metal/semiconductor interface. At the wavelength of 625 nm, the situation reverses and the wider nanobeams display a resonantly-enhanced absorption with a $\eta_{\text{abs}} \approx 3$. More subtly, the blue and red absorption spectrums indicate a suppressed absorption in one nanobeam when the other is on resonance. This is highly desirable to reduce any unwanted cross-talk between neighboring pixels that are designed to collect light at distinct wavelengths. Next, we describe how these useful spectral splitting properties arise from the optical coupling between neighboring nanowires in the bi-grating.

In an effort to understand the possible ways the semiconductor nanobeams can optically couple, previous studies on the light scattering from closely-spaced metallic nanoparticle pairs and ensembles provide valuable guidance. For such systems, it has been demonstrated that both near- and far-field coupling can influence the scattering process. An overlap of the excited near-fields of the particles can result in coupled bonding and anti-bonding plasmon oscillator modes that feature resonance frequencies that are shifted from the individual particle resonances. Recently, such near-field coupling was also observed for high-index semiconductor nanostructures and linear-combination-of-atomic-orbital style models were developed to describe the observed resonance frequency shifts. Closely-spaced metal particles are also known to affect each other's radiation to the far-field and both superradiant and subradiant behavior has been observed depending on the particle spacing. Physically, this coupling is mediated by the scattered fields produced by the particles and superradiance and subradiance is achieved when these fields interfere

constructively or destructively in the far-field. For such systems, this coupling is described in terms of an anti-Hermitian coupling matrix that links the quasi-bound states. In keeping with this particular viewpoint, we employ temporal coupled mode theory (CMT) to derive a matrix equation that describes the optical excitations in a metafilm supporting two coupled resonances in the wide and narrow nanowires. If we assume that these resonances are accessed via a single incidence/exit channel for the light, we can write:

$$\frac{\partial}{\partial t} \begin{bmatrix} \mathbf{c}_1 \\ \mathbf{c}_2 \end{bmatrix} = j \begin{bmatrix} \omega_1 + j(\gamma_{a1} + \gamma_{r1}) & \omega_{12} + j\gamma_0 \\ \omega_{12} + j\gamma_0 & \omega_2 + j(\gamma_{a2} + \gamma_{r2}) \end{bmatrix} \begin{bmatrix} \mathbf{c}_1 \\ \mathbf{c}_2 \end{bmatrix} + \begin{bmatrix} \kappa_1 \\ \kappa_2 \end{bmatrix} S_+ \quad \text{Eq.(8)}$$

where S_+ are the incident amplitude normalized such that $|S_+|^2$ denotes the incident power and \mathbf{c}_i 's are the amplitudes in each modes with $|c_i|^2$ corresponds to the stored energy. κ_i quantify the coupling to these modes to external radiation. ω_i , γ_{ai} and γ_{ri} in the diagonal terms represent resonance frequencies, absorption loss and radiation loss, respectively. The off-diagonal terms represents the interaction between the two coupled resonators. Whereas the first off-diagonal term ω_{12} quantifies the direct near-field coupling, the second part (γ_0) quantifies the indirect far-field coupling that is dependent on the radiation from the two resonances as $\gamma_0 = \sqrt{\gamma_{r1}\gamma_{r2}}$. The relative phase of the radiation fields between the two modes determines whether beams will aid or suppress each other's radiation to the far-field.

Akin to metallic nanoparticles, the considered semiconductor nanobeams support very low radiative quality (Q) factor antenna modes and are thus expected to also feature near-field and far-field, radiative coupling. In our designed device, the metallic fins between semiconductor beams suppress the near-field coupling. As a result, the interaction occurs primarily through far-field coupling. We will illustrate how the far-field coupling of the scattered fields from the narrow and wide beams can be used to spectrally sharpen the absorption properties as compared to individual beams. The most effective far-field coupling is achieved when the beams scatter light into a single optical mode/channel. Figure 13f shows a simulation of the scattered electric field at a selected wavelength of 605 nm, centered between the resonant wavelengths of the wide and narrow beams. It can be seen that the scattered fields emerging from the differently-sized beams feature an approximately π phase difference, consistent with the CMT. At a small distance from the surface, one can observe flat, horizontal phase fronts of a single outgoing plane wave that results from the coherent addition of the scattered field from the wide and narrow beams. Given the fact that there is only one outgoing plane-wave channel, it is possible to capture the optical properties of the bi-grating with Eq.8. The nanobeam spacing controls the number of channels by which light can excite/escape the bi-grating structure. As such, this parameter can have a significant impact on the absorption spectrum. The type of changes that can be achieved in terms of the spectral absorption properties of the metafilm are discussed in the next section.

Figure 14a shows how, for a pitch $P = 350$ nm between adjacent nanobeams, the absorption spectrums of the narrow and wide beams feature Lorentzian lineshapes and the spectrums significantly overlap. This pitch is sufficiently large to allow for the generation of first-order diffracted beams. As a result, the interference/coupling of scattered fields from the differently-sized beams is weak. The absorption spectrums significantly change when we reduce the pitch to 160 nm, as seen in the Fig. 14b. For such a small pitch, the absorption spectrums feature asymmetric lineshapes and a reduced spectral overlap.

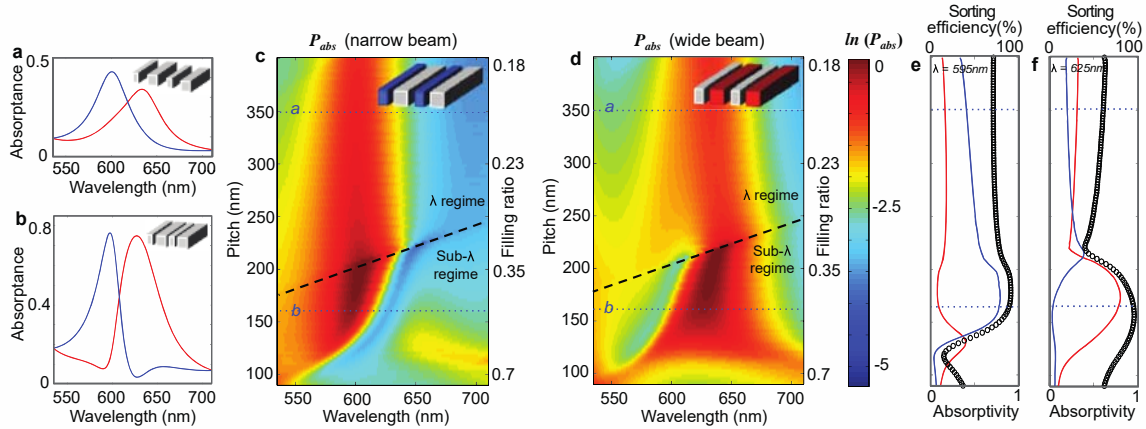


Fig 14. Origin and effectiveness of anti-Hermitian coupling in a semiconductor nanobeam array with two beam widths. (a, b) Absorption spectrums of arrays that feature (a) supra- and (b) sub-diffraction limit pitches of 350 nm and 160 nm respectively between adjacent beams. (c, d) Maps of the spectral absorption in just (c) the narrow or (d) the wide nanobeams versus array pitch. The black dashed line indicates the boundary below which first-order diffraction is precluded and a metamaterial description becomes valuable. In this regime, pronounced spectral enhancements and suppressions in the absorption are observed. The blue dotted lines indicate the locations at which spectrums shown panels a and b were taken. (e, f) Vertical cross sections of the maps in panels c and d taken at the wavelengths of (e) 595 nm and (f) 625 nm respectively. Blue line shows the absorption in the narrow beams (P_{narrow}) and the red line shows the absorption in wide beams (P_{wide}). Black circled curve depicts the sorting efficiency defined as the ratio of the absorbed power in the target beam of the total absorbed power η_s (%) = $[P_{\text{target}} / P_{\text{total}}] \times 100$, Although the efficiency is over 50% for most periods, it reaches near 100% at in metamaterial regime with P_{total} also being close to unity.

At this pitch, no first-order diffraction occurs and the two resonant beams are strongly coupled via the single exit channel. From Eq.8 it is clear that in the absence of near-field coupling and with a phase difference of π in the far-field coupling, the off-diagonal terms in the matrix in Eq.8 are purely imaginary with both a positive sign. This type of subradiant coupling reduces the radiation leakage (i.e. increases the radiation Q_{rad}) and thus increases the local energy storage. Between the resonances, the overall absorption is maximized and close to unity as the scattered fields from the two beams destructively interfere to prevent the generation of a substantial reflected wave. It is also important to note that this type of coupling does not modify the spectral location of the resonance frequencies of the individual beams. On resonance of the narrow beams, the energy storage and thus the light absorption in these beams is maximized. The action of the wide beams is to enhance the energy storage and absorption in the narrow beams by reducing the radiation leakage. This is consistent with the powerflow map shown in Fig.13d that shows that light enters the slit from a larger absorption cross section. The absorption cross section of the narrow beams can be so large as to reduce the absorption in the wide beams. This results in a very high sorting efficiency, where virtually all of the incident photons are absorbed in the resonant beam and a very small fraction is absorbed in the off-resonant beam. A similar physical effect emerges in reverse when the wide beam is excited on resonance.

The benefits of subwavelength scaled devices for spectral sorting are more obviously illustrated in Figs 14c,d that map the changes in the spectral absorption of the nanobeam-array as the pitch is tuned. The absorbed fraction in the narrow nanobeams is shown in Fig 14c and the absorbed fraction in the wide nanobeams is shown in Fig. 14d. In the regimes below the black dashed lines in both maps, the bi-gratings operate as a metafilm for which the formation of first-order diffracted beams is precluded. This results in effective far-field coupling through a single radiation channel and a more effective sorting of photons into resonant beams. In very deep subwavelength regime where the pitch between adjacent nanobeams is less than 100 nm, near-field interaction starts to play a significant role and spectral mode splitting is observed.

To quantify how effectively this system is able to spectrally sort light, we define the sorting efficiency (η_s) as the fraction of absorption at the targeted beam array (P_{target}) over the total absorption in silicon (P_{total}), i.e. η_s (%) = $[P_{target} / P_{total}] \times 100$. The sorting efficiency at two closely-spaced target wavelengths of 595 nm and 625 nm are plotted against the pitch in Figs 14e,f. From these figures, it is clear that the sorting efficiencies reach almost 100% in the metafilm regime. The absolute value of absorbed fraction is approximately 0.8 for pitches between 150 nm and 200 nm, as shown by the solid red and blue lines. On the other hand, as the pitch size is increased to supra-wavelength values, the achievable sorting efficiencies and overall light absorption significantly decrease.

Lastly, we experimentally demonstrate the spectral sorting capabilities of bi-grating devices. We start by analyzing two reference devices that feature arrays with single-sized nanobeams that have widths of either 60 nm or 80 nm. Figures 15a,b show calculated and experimental reflection spectrums from the corresponding devices. The solid line in Fig. 15a shows the simulated reflection spectrum using finite-difference time-domain (FDTD) simulations (Solid line). Each spectrum displays a single reflection dip at a resonant wavelength that is determined by the beam width. This dependence follows from a simple Fabry-Perot style model for groove resonances where trapped light can circulate between the base and exit of the groove that serve as closed and open reflection boundaries, respectively. In such a case, the lowest-order resonance is expected when the free space wavelength equals $\lambda = 4nd$, where d is the groove depth and n is the mode index of the guided mode supported by the groove. Here, we have to consider the properties of the excited transverse magnetic (TM_1) mode with one anti-node of the electric field in the center of the guide. Its mode index increases with increasing width and the resonance for the wider groove is thus redshifted (as opposed to the dependence seen for gap plasmon resonances on grooves width). The spectral dependence of the reflectivity can be described nicely by a coupled mode theory (CMT) for a system supporting a single resonance that is coupled to a single input/output channel. From the fits one can then extract useful physical parameters to understand the system operation. For example, for the narrow beam device simulation, the best agreement between the FDTD and CMT is obtained for a radiation loss rate $\gamma_r = 6.82 \times 10^{13} \text{ s}^{-1}$ and an absorption loss rate $\gamma_a = 4.8 \times 10^{13} \text{ s}^{-1}$. The close match between the radiation and absorption loss rates indicates that the system is near-critical coupling and therefore exhibits near-unity absorption on resonance. The single reflection dip at the target wavelength is also experimentally demonstrated in fabricated narrow-beam and wide-beam devices, as seen in Fig. 15b. Minor discrepancies between experiment and theory, i.e. the experimental non-zero reflection dip with a larger full-width

at half-maximum are attributed to slight shape and size variations in the fabricated nanobeams and to non-perfect normal-incident illumination.

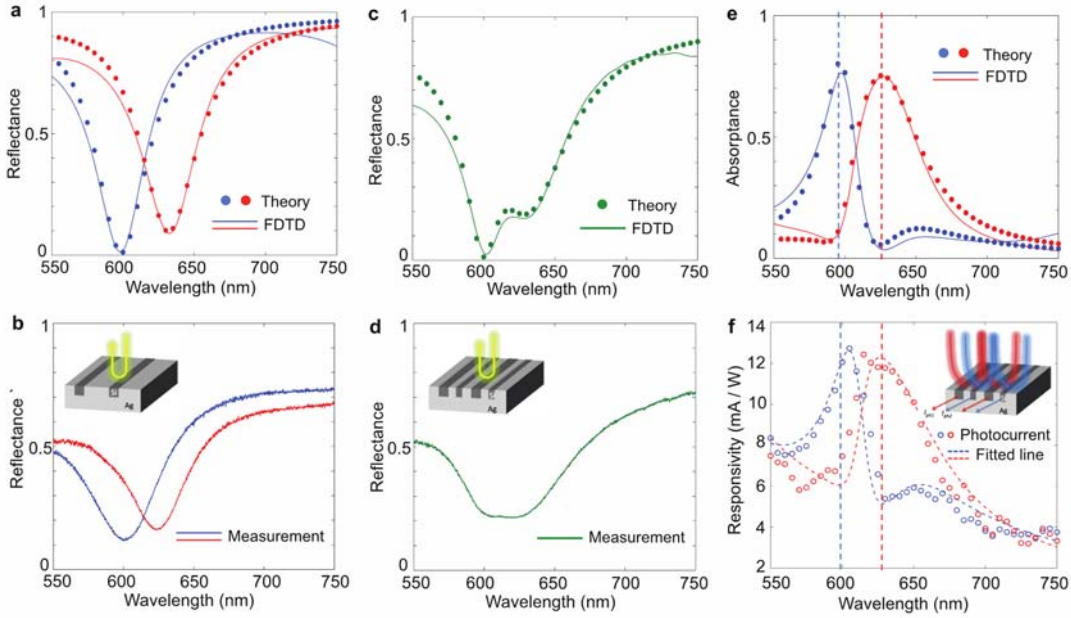


Fig 15. Experimental demonstration of spectrally sorted photocurrent generation in anti-Hermitian metafilm device. (a, b) Reflection spectrums of single-sized nanobeam arrays obtained by coupled mode theory (CMT) and finite-difference time-domain (FDTD) simulations (a) and in experiments (b) for beam widths of 60nm (blue) and 80 nm (red), respectively. (c, d) Reflection spectrums of two type of the nanobeams in a and b interlaced at a subwavelength scale in theory with simulation (c) and in experiments (d). (e) Absorption spectrum of the multi-sized nanobeam array of c and d as calculated using CMT and FDTD simulations. Fraction of the absorption is shown in blue for narrow and red for wide nanobeam array. (f) Experimentally extracted photocurrent spectrum depicted as circled point with the fitted line for an anti-Hermitian coupled system. Photocurrent in differently-sized nanobeams is extracted separately and measured as seen in blue and red color.

Figure 15c,d show the simulated and measured spectral reflectance for a bi-grating with 60 nm and 80 nm beams interlaced. A suppressed reflection can be observed around the resonant wavelengths of the 60 nm and 80 nm beams. The simulated spectrum as calculated by the FDTD technique can nicely be reproduced using CMT with the same values of γ_r and γ_a as obtained for the single-sized nanobeams. Additionally, we extracted the strength of the indirect far-field coupling γ_0 between the resonances supported by the two beam sizes. Such a model generates scattered fields from the two beams with a phase difference equal to π across the resonant dip. The large phase difference between the scattered fields from the beams implies effective anti-Hermitian coupling linked to a destructive far-field interference.

Whereas it is challenging to resolve the individual resonances in a far-field reflection spectrum, photocurrent measurements can access the near-fields in the two beams and demonstrate spectral sorting of light (Fig. 15e,f). Figure 15e shows the absorption in the narrow and wide nanobeams as simulated by FDTD and as determined by CMT using the same coupling parameters used in Fig. 15c. The experimental spectral dependence of the photocurrent in each of the sets of beams is also plotted in Fig. 15f. Note

that photocurrent spectrums were measured separately from the narrow beams and wide beams under the monochromatic illumination with a tunable light source. For each of the two beam widths a clear maximum in the photocurrent is observed near the resonance wavelength for that width. A suppression in the photocurrent is also seen near the resonance wavelength of the wider beam. The observation of asymmetric photocurrent peaks also matches well to the anti-Hermitian model fits shown as red and blue dashed lines. In the experimental case, the overall current increases on the short wavelength-side of the spectrum due to the stronger intrinsic absorption than predicted by the CMT. The measured peak responsivity is around 12 mA/W and can be increased through an improved electrical device design, involving electrical doping and improved surface passivation of the NWs. It is also worth noting that this type of spectral sorting is not limited to two sorted wavelengths. By designing metafilms with a larger number of differently-sized nanobeams, one can achieve sorting of more wavelengths. Such designs can find potential applications in next-generation solar cells, where the power conversion efficiency can be enhanced through a full utilization of the solar spectrum by directing light of different wavelength ranges into different semiconductor materials with distinct bandgaps. The presented lateral sorting by wavelength is quite distinct from the spectral sorting of light in the stacked layers of multi-junction solar cells.

To summarize, we have demonstrated anti-Hermitian coupling in semiconductor metafilms to design an efficient and integrated photon-sorting detector. By judiciously engineering nanobeam arrays at a deep-subwavelength scale, these metafilm devices can effectively operate similarly to open quantum system with two resonances that interact via the far-field radiation continuum. This affords realization of compact optoelectronic devices that function both as photon-sorters and photodetectors in a single, ultrathin layer. Such devices can find application in the field of bio-sensing, energy harvesting, and optical communication.

II.7 Cathodoluminescence Characterization of Metamaterial Building Blocks.

The successful realization of future, ultra-compact photonic devices will require the development of new techniques capable of correlating the nanostructural properties of materials and devices to their optical performance. In collaboration with Albert Polman's group at the FOM-Institute in the Netherlands, we have used utilize electron-beam based techniques that can simultaneously map the morphology and optical modes of plasmonic nanocavities and antennas at very high spatial resolution. An example structure that we pursued is a metallic nanowire antenna that constitutes a basic building block of a plasmonic metasurface.

From a fundamental perspective, 1D plasmonic cavities are attractive candidates for study, because their simplicity allows a comprehensive understanding of the antenna's behavior in both the near- and far-field. For all wavelength-scale optical structures resonance will be achieved when the structure supports a standing wave. This occurs when the structure has a confined optical mode which makes a round-trip through the structure and in so doing accumulates an amount of phase equal to an integer multiple of 2π . In 1D surface plasmon polariton (SPP) cavities, this phase accumulation is well known and can be written in a simple Fabry-Pérot equation:

$$\phi_{total} = m * 2\pi = \vec{k}_{spp} * 2L + 2\phi_r \quad \text{Eq.(9)}$$

There are two primary components to the phase accumulation: that acquired during propagation, which depends on the plasmon wavevector k_{SPP} and the cavity length L ; and the discrete phase accumulation on reflection ϕ_r . The second term differentiates the behavior of optical frequency dipole antennas from microwave and radiowave analogues, in which the phase pickup on reflection is negligible. Other authors have made a mathematically similar treatment in which the correction is added to the cavity's length L , rather than to the round-trip phase. The phase pickup approach is more similar to that considered in microwave engineering, and can be intuitively understood as arising from the impedance matching condition between the confined SPP propagating inside the cavity with the propagating waves in the surrounding dielectric environment. Most of the systems considered so far are simple 1D SPP waveguides, either strips or wires, truncated abruptly with a free-end. The dimensions of this reflector are far below the wavelength-scale, so a full calculation of the phase-pickup also must take into account the field overlap between the confined wave at the truncation with that of the propagating waves in free space²⁸. For this reason, one would expect the phase pickup to depend sensitively on the exact geometry of this end facet or termination of the waveguide. This discrete reflection phase ϕ_r can in principle vary over a 2π range, so in small cavities at low mode order m , it will be similar in magnitude to the phase accumulation during propagation, so it must be understood and controlled in order to engineer cavities with chosen resonant frequencies. The current method for experimentally determining ϕ_r is to construct a resonant cavity with a known SPP dispersion and measure its resonant frequencies, then to calculate ϕ_r from Eq.(9). This method has been successfully employed, but suffers from several drawbacks, since it depends on knowledge of the SPP dispersion and only produces values for ϕ_r at the resonant frequencies of the antenna.

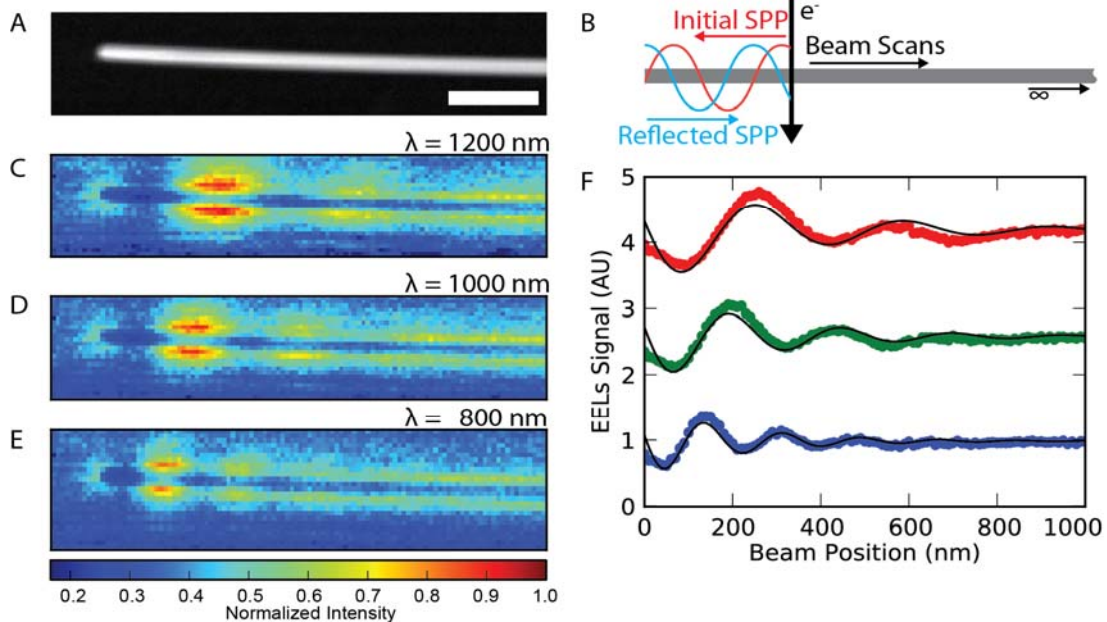


Figure 16. SPP Reflections from a single truncation in TEM EELS. A) A TEM image of a long silver nanowire near one open end. B) Schematic of the measurement. C-E) Mode density maps of the NW in A, taken at 3 different free space wavelengths, 1200, 1000, and 800 nm. F) Line scan representations of the images C,D,E. The attenuated oscillations observed can be fit with a simple model, described in the text. The model fit is show by solid black lines.

In this program, we performed a detailed examination of how the entire complex reflectivity, including the reflection phase and amplitude, can be measured over a broad frequency range spanning the visible and near infrared with electron energy loss spectroscopy (EELS) in a canonical surface plasmon polariton (SPP) cavity, a finite length chemically synthesized silver nanowire (See Fig. 16). This was done by researchers funded by this program and the MURI on quantum metamaterials led by Prof. Rashid Zia and supervised by Dr. Gernot Pomrenke.

II.7 References

1. Kildishev, Alexander V. Boltasseva, A. & Shalaev, V. M. Planar Photonics with Metasurfaces. *Science* **339**, 1232009 (2013).
2. Vahala, K. J. Optical microcavities. **424**, (2003).
3. Kats, M., Blanchard, R., Genevet, P. & Capasso, F. Nanometre optical coatings based on strong interference effects in highly absorbing media. *Nat. Mater.* **11**, 1–5 (2013).
4. Gires, F. & Tournois, P. Interferometre utilisable pour la compression d'impulsions lumineuses modulees en frequence. *C. R. Acad. Sci. Paris* **258**, 6112–6115 (1964).
5. Dotan, H. *et al.* Resonant light trapping in ultrathin films for water splitting. *Nat. Mater.* **12**, 158–64 (2013).
6. Chipouline, a., Simovski, C. & Tretyakov, S. Basics of averaging of the Maxwell equations for bulk materials. *Metamaterials* **6**, 77–120 (2012).
7. Cao, L. *et al.* Engineering light absorption in semiconductor nanowire devices. *Nat. Mater.* **8**, 643–7 (2009).
8. Lin, D., Fan, P., Hasman, E. & Brongersma, M. L. Dielectric gradient metasurface optical elements. *Science* **345**, 298–302 (2014).
9. Brongersma, M. L., Cui, Y. & Fan, S. Light management for photovoltaics using high-index nanostructures. *Nat. Mater.* **13**, (2014).
10. Cao, L., Park, J.-S., Fan, P., Clemens, B. & Brongersma, M. L. Resonant germanium nanoantenna photodetectors. *Nano Lett.* **10**, 1229–33 (2010).
11. Biener, G., Niv, A., Kleiner, V. & Hasman, E. Metallic subwavelength structures for a broadband infrared absorption control. *Opt. Lett.* **32**, 994–996 (2007).
12. Woltersdorff, V. W. The optical constants of thinner metal layers in the infrared long wavelength. *Zeitschrift fur Phys.* **91**, 230–252 (1934).
13. Fante, R. L. & McCormack, M. T. Reflection properties of the Salisbury screen. *IEEE Trans. Antennas Propag.* **36**, 1443–1454 (1988).
14. Kim, S. J. *et al.* Superabsorbing, artificial metal films constructed from semiconductor nanoantennas. *Nano Lett.* **16**, 3801–3808 (2016).
15. Brongersma, M. L. Plasmonic Photodetectors, Photovoltaics, and Hot-Electron Devices. *Proc. IEEE* **PP**, (2016).

III. Personnel and Training Opportunities

III.1. Personnel Supported

At Stanford University, this program supported research in the group of Prof. Mark L. Brongersma (PI). At different times, it funded work by a student Soo Jin Kim and postdoc Dr. David Schoen and Dr. Juhyung Kang. The researchers were together working on several projects aimed at the development of metamaterial building blocks and devices.

III.2. Research Training of Students

The training of graduate students and postdoctoral researchers was a critical aspect of this project. The sudden burst of activity in the field of metasurface and metafilms has led to hundreds of publications in the international literature and popular press. New conferences and symposia are devoted to just this topic (a number organized by the PIs). Major companies, such as Northrop Grumman, Samsung, and Hewlett Packard now have active research efforts in this field of study.

IV. Dissemination of Research findings

IV.1. Publications, Books, and Presentations

The research from this program led to a total of 5 publications in refereed journals and one that is currently under review. The PI also gives more than 15 invited talks (including several keynotes) each year on the topics related to this program. He also incorporated the material from this program into a short courses taught at the CLEO conference every year on plasmonics. The students funded by this effort presented a number of contributed talks at International conferences.

Publications in 2015

1. Park, J., Kang, J., Kim, S. J., Hasman, E. & Brongersma, M. L. Tuning Optical Absorption in an Ultrathin Lossy Film by Use of a Metallic Metamaterial Mirror. *IEEE Photonics Technol. Lett.* 27, 1617–1620 (2015).
2. Ee, H.-S., Kang, J.-H., Brongersma, M. L. & Seo, M.-K. Shape-dependent light scattering properties of subwavelength silicon nanoblocks. *Nano Lett.* 15, 1759–1765 (2015).
3. Schoen, D. T., Atre, A. C., García-Etxarri, A., Dionne, J. A. & Brongersma, M. L. Probing Complex Reflection Coefficients in One-Dimensional Surface Plasmon Polariton Waveguides and Cavities Using STEM EELS. *Nano Lett.* 15, 120–126 (2015).

Publications in 2016

4. Kim, S. J. et al. Superabsorbing, artificial metal films constructed from semiconductor nanoantennas. *Nano Lett.* 16, 3801–3808 (2016).
5. Brongersma, M. L. Plasmonic Photodetectors, Photovoltaics, and Hot-Electron Devices. *Proc. IEEE PP*, (2016).

Publications in 2017

6. Soo Jin Kim, Ju-Hyung Kang, Mehmet Mutlu, Joonsuk Park, Woosung Park, Kenneth E. Goodson, Robert Sinclair, Shanhui Fan, Pieter G. Kik, and Mark L.

Brongersma, “Anti-Hermitian Photodetector Facilitating Efficient Subwavelength Photon-sorting”, under review in Nature Communications 2017.

IV.2. Interactions and Transitions

This project has created a number of exciting opportunities for knowledge transfer. The work on integrated detectors has attracted the interest of several solar companies and we Enel Green Power and Metamaterials Technology Incorporated may adopt some of the developed technology. The work on Si blocks is of interest to an augment reality company, Magic Leap and they are now funding a project on eye tracking with Si nanostructure metasurface components. This could also impact the MURI program on metasurfaces led by Professor Federico Capasso and supervised by Dr. Gernot Pomrenke. Knowledge transfer also occurred via individual interactions, presentations, and short courses.

IV.3. Honors and Awards

Brongersma served as the Chair for the Gordon Research Conference on Plasmonics. He also has become Deputy Director for the Geballe Laboratory for Advanced Materials at Stanford. In 2016, Brongersma was elected as a Director-at-large of the Optical Society Board of Directors (2016). He has continued this function in 2017.